Column Relative Humidity and Primary Condensation Rate as Two Useful Supplements to Atmospheric River Analysis

Ruping Mo[1], Rita So[1], Melinda M. Brugman[1], Curtis Mooney[2], Anthony Q. Liu[2], Matthias Jakob[3], Armel Castellan[4], and Roxanne Vingarzan[5]

[1]National Laboratory-West, Environment and Climate Change Canada, Vancouver, BC, Canada
[2]National Laboratory-West, Environment and Climate Change Canada, Edmonton, Alberta, Canada
[3]BGC Engineering, Vancouver, BC, Canada
[4]Client Services, PSOW, Environment and Climate Change Canada, Victoria, BC, Canada
[5]Applied Sciences, PSOW, Environment and Climate Change Canada, Vancouver, BC, Canada

Key Points:

- Many heavy precipitation events can be attributed to the strong water vapor convergence induced by atmospheric rivers
- The column relative humidity and the primary condensation rate are proposed as two supplements to the standard weather analysis to help focus on the atmospheric river contribution to heavy precipitation
- The primary condensation rate can be used as a proxy for the large-scale precipitation rate and has the application potential in storm scaling and classification

Corresponding author: R. Mo, ruping.mo@ec.gc.ca

Abstract

Landfalling atmospheric rivers (ARs) frequently trigger heavy and sometimes prolonged precipitation, especially in regions with favored orographic enhancement. The presence and strength of ARs are often described using the integrated water vapor (IWV) and the integrated vapor transport (IVT). However, the associated precipitation is not directly correlated with these two variables. Instead, the intensity of precipitation is mainly determined by the net convergence of moisture flux and the initial degree of saturation of the air column. In this study, a simple algorithm is proposed for estimating the heavy precipitation attributable to the IVT convergence. Bearing a strong resemblance to the Kuo-Anthes parameterization scheme for cumulus convection, the proposed algorithm calculates the large-scale primary condensation rate (PCR) as a proportion of the IVT convergence, with a reduction to account for the general moistening in the atmosphere. The amount of reduction is determined by the column relative humidity (CRH), which is defined as the ratio of IWV to its saturation counterpart. Our analysis indicates that the diagnosable PCR compares well to the forecast precipitation rate given by a numerical weather prediction model. It is also shown that the PCR in an air column with CRH < 0.50 is negligibly small. The usefulness of CRH and PCR as two complements to standard AR analysis is illustrated in three case studies. The potential application of PCR to storm classification is also explored.

1 Introduction

Water vapor forms the link between the Earth's surface and the atmosphere in the hydrologic cycle, and plays an important role in various atmospheric processes such as cloud formation, precipitation, energy transfer and conversion, radiation and climate change (Espy, 1841; Tyndall, 1863; McEwen, 1930; Houghton, 1951; Manabe & Wetherald, 1967; Jacob, 2001; Schneider et al., 2010). Because the moisture distribution is highly non-homogeneous both in space and time, water vapor transport is essential in shaping the global energy and water cycles. It has been demonstrated that a substantial fraction of the water vapor transport in the extratropical atmosphere can be attributed to a phenomenon called "atmospheric river" (AR), which is a long and narrow moist flow in the atmosphere that may carry as much water as the Amazon River (Newell et al., 1992; Zhu & Newell, 1994, 1998). The AR development is typically associated with a low-level jet stream ahead of the cold front of an extratropical cyclone, and frequently leads to heavy precipitation

at locations where the moist flow is forced upward by mountains or frontal systems (Ralph et al., 2004; Neiman et al., 2008; Lavers et al., 2011; Garreaud, 2013; Mahoney et al., 2016; Paltan et al., 2017; Blamey et al., 2018; Guan & Waliser, 2019; Mo et al., 2019; Sharma & Déry, 2020; Ye et al., 2020; Xiong & Ren, 2021; Zheng et al., 2021; American Meteorological Society, 2021). Note that, before the term AR was coined by Zhu and Newell (1994), the phenomenon was also known as the "warm conveyor belt" (Browning, 1971; Harrold, 1973; Carlson, 1980) or the "moist tongue" (Rossby & Collaborators, 1937).

The two commonly used fields to detect and define ARs are the vertically integrated water vapor (IWV) and the integrated vapor transport (IVT) (Newell et al., 1992; Zhu & Newell, 1998; Dettinger, 2004; Ralph et al., 2004; Lavers et al., 2012; Wick et al., 2013; Guan & Waliser, 2015, 2019; Pan & Lu, 2019). The IWV is also known as precipitable water vapor. It can be calculated from a moisture profile alone, and its value indicates the total water vapor content in a vertical air column. The use of IWV as a proxy for AR detection was established by Ralph et al. (2004) based upon its close correlation with IVT over the extratropical North Pacific. When both wind and moisture profiles are available, it is more appropriate to analyze ARs based on the IVT distribution. Recently, Ralph et al. (2019) introduced a scale for characterizing the strength and potential impacts of ARs based on the IVT intensity and the event duration. This 5-category scale has been widely used to communicate the benefits and hazards associated with ARs (Cruickshank, 2019; Zhang et al., 2019; Hatchett et al., 2020; Zhao, 2020).

The major impact of an AR is to produce large amounts and often high-intensity precipitation. These precipitation events, often in combination with snowmelt, can lead to numerous hazards, including flooding, washouts, river bank erosion, channel scour, landslides, and avalanches. These hazards can lead to severe economic losses and fatalities where they intercept development and infrastructure. They can also cause major environmental damage, for example, through a landslide, or the severing of an oil pipeline. Hence, accurate storm prediction is of paramount importance even for remote communities. However, neither the IWV nor the IVT can quantify the precipitation intensity. Precipitation received at a location is mainly controlled by three factors: 1) the IWV, which accounts for the total amount of moisture in the atmosphere; 2) the relative moistness of the air column; 3) the presence of physical mechanisms leading to condensation and precipitation (Tuller, 1971, 1973). In a motionless atmosphere, the IWV value could be used to represent the potential maximum amount of precipitation if all the vapor above

the Earth's surface was condensed and precipitated out. However, depending on the degree of saturation of the air column, the actual amount of condensation often accounts for only a small fraction of the IWV. The saturation level is determined by the vapor content in the air and the temperature profile. In reality, the amount of water vapor in an air column constantly changes due to moisture transport. Since the IWV does not account for additional water vapor advected into the column, it cannot estimate the actual precipitation amount (Tuller, 1973; Stull, 2017). In actual heavy precipitation events, the storm-total precipitation amounts are often much larger than the highest IWV measured in the storm period. This is due to the flow convergence that brings the water vapor into the storm from a much larger surrounding area.

The IVT is a measure of overall strength of horizontal moisture flux. It is reasonable to expect that stronger IVT could bring more water vapor to an area and thereby lead to heavier precipitation. However, the IVT value and the quantity of precipitation can be poorly related, because precipitation is associated with net convergence of water vapor flux rather than with moisture transfer (Benton & Estoque, 1954). Furthermore, the converged water vapor will be shared between condensation and a general moistening of the atmosphere, and the fraction of condensation depends on the degree of air column saturation (Kuo, 1974; Anthes, 1977; Sundqvist, 1978).

The main purpose of this paper is twofold: (i) to promote the use of the column relative humidity (CRH) as an appropriate measure of air column saturation (Bretherton et al., 2004); and (ii) to propose an algorithm to diagnose the primary condensation rate (PCR) attributed to the horizontal moisture flux convergence, which can be used to estimate the AR contribution to heavy precipitation. To quantify the concept of converged water vapor shared between condensation and air moistening (Sundqvist, 1978), the PCR is defined as a function of the CRH and the net convergence of horizontal water vapor flux. It can be used as a proxy for the large-scale precipitation rate when condensed-water storage is neglected. The algorithm for calculating PCR bears a strong resemblance to the Kuo-Anthes parameterization scheme (Anthes, 1977), which depends on the occurrence of large-scale convergence to cumulus convection. Both CRH and PCR are diagnosable variables that can complement AR analysis.

The rest of the paper is organized as follows. Section 2 describes the data used in this study and the AR identification methods. Section 3 reviews the balance requirements

for water in the atmosphere and gives the definitions of PCR and CRH. Three case studies are provided in Section 4 to illustrate how to make use of PCR and CRH in AR analyses. The potential application of PCR to storm scaling is explored in Section 5. Further discussion and conclusions are given in Section 6.

2 Data Description and Atmospheric River Identifications

2.1 Data Sources

The model data used in this study are mainly extracted from the analyses and predictions of the operational Global Deterministic Prediction System (GDPS) of Environment and Climate Change Canada (ECCC). This numerical weather prediction (NWP) model uses a Yin-Yang grid with an approximate horizontal spacing of 15 km and an 84-level terrain-following, staggered log-hydrostatic-pressure vertical coordinate system (McTaggart-Cowan et al., 2019). It is currently run twice daily starting at 0000 and 1200 UTC, respectively. This model uses the modified Sundqvist scheme for grid-scale condensation parameterization, which assumes that the precipitating hydrometeors fall instantaneously to the ground. It uses a legacy grid-scale cloud scheme (Sundqvist et al., 1989) to predict large-scale clouds. In addition, three different parameterization schemes are employed to handle deep, shallow, and elevated convection.

Other data include a weather radar mosaic obtained from the China Meteorological Administration (`http://en.weather.com.cn/radar/`) and a Prince George radar image from the Canadian Historical Weather Radar Archive (`https://climate.weather.gc.ca/radar/index_e.html`). Hourly precipitation amounts observed at weather stations across British Columbia (BC) are obtained from the ECCC data archive, the BC Wildfire Service (`https://www2.gov.bc.ca/gov/content/safety/wildfire-status/wildfire-situation/fire-weather`) and the BC Ministry of Transportation and Infrastructure (`https://prdoas6.pub-apps.th.gov.bc.ca/saw-paws/weatherstation`).

2.2 Methods of AR Identification: IWV and IVT

The increasing interest in ARs has led to the development of many novel and objective AR identification methods (Shields et al., 2018). The two most common fields used to identify ARs are IWV and IVT, which can be defined in a pressure (p) coordi-

nate system as follows

$$\text{IWV} = W = \frac{1}{g}\int_{p_\text{t}}^{p_\text{b}} q\mathrm{d}p, \quad \text{IVT} = |\mathbf{Q}|, \quad \text{with } \mathbf{Q} = \frac{1}{g}\int_{p_\text{t}}^{p_\text{b}} q\mathbf{V}_\text{h}\mathrm{d}p, \tag{1}$$

where g is the acceleration due to gravity, q is the specific humidity, $\mathbf{V}_\text{h}$ is the horizontal wind vector, and p_b and p_t are the pressures at the bottom and the top of the air column, respectively. The vector $\mathbf{Q}$ is called the integrated water vapor flux (IWVF). The IVT is defined as the magnitude of IWVF. For brevity, we also use W as a mathematical symbol to represent the IWV in the equation.

Water can also be stored in the atmosphere in condensed (liquid and/or solid) phase. Therefore, the vertically integrated condensed water (ICW) and the integrated condensed water flux ($\mathbf{Q}_\text{c}$) can be similarly expressed by (e.g., Peixoto, 1973, Eq. 16b)

$$\text{ICW} = W_\text{c} = \frac{1}{g}\int_{p_\text{t}}^{p_\text{b}} q_\text{c}\mathrm{d}p, \quad \mathbf{Q}_\text{c} = \frac{1}{g}\int_{p_\text{t}}^{p_\text{b}} q_\text{c}\mathbf{V}_\text{h}\mathrm{d}p, \tag{2}$$

where q_c is the specific amount of water in the condensed phase. In the atmosphere, the storage of water in the vapor phase is much larger than in the condensed phase (Peixoto, 1973). Therefore, it can be expected that IWV $\gg$ ICW and $|\mathbf{Q}| \gg |\mathbf{Q}_\text{c}|$.

Ralph et al. (2004) proposed a simple method for AR identification based on the IWV distribution: an AR is an elongated moisture plume with core IWV values exceeding 20 kg m^{-2} for $\geq$ 2000 km in the along-plume direction and $\leq$ 1000 km in the cross-plume direction. ARs can also be identified based on the IVT distribution, such as an elongated area with a minimum IVT threshold of 250 (or 500) kg m^{-1}s^{-1}, a length $\geq$ 2000 (or 1500) km, and a length-to-width ratio > 2 (e.g., Rutz et al., 2014; Guan & Waliser, 2015; Mahoney et al., 2016).

In theory, the vertical integration should be carried out from the Earth's surface to the top of the atmosphere ($p_\text{t} = 0$). However, since q decreases rapidly with height, integration up to the 300-hPa level usually suffices for practical applications (Zhu & Newell, 1998; Lavers et al., 2012). As an example, Fig. 1 plots the radiosonde profiles at Port Hardy, BC, Canada, valid at 1200 UTC 27 November 2020. The air temperature (T) and dewpoint (T_d) profiles in Fig. 1a indicate that the air column in the troposphere was quite moist, especially in the layer below 500 hPa where $T - T_d \leq 2$°C. In Fig. 1b, both the specific humidity q and the saturation specific humidity q_s are very close to zero above the 300-hPa level; the formulas for calculating q and q_s are given in Appendix A.

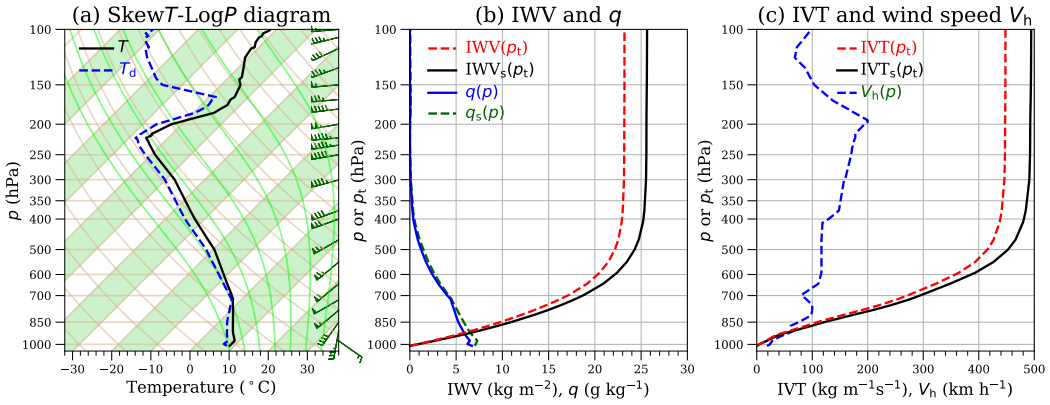

Figure 1. Upper-air analysis based on a sounding taken at Port Hardy, BC, Canada (CYZT: 50.68°N, 127.36°W), valid at 1200 UTC, 27 November 2020. (a) The profiles of temperature (T), dewpoint (T_d), and wind vectors in the Skew$T$-Log$P$ diagram with a 45° rotation of isotherms relative to horizontal; T and T_d are in Celsius (°C). (b) The profiles of specific humidity (q), saturation specific humidity (q_s), integrated water vapor (IWV), and integrated saturation water vapor (IWV$_\mathrm{s}$). (c) The profiles of wind speed (V_h), integrated vapor transport (IVT) and its saturation counterpart (IVT$_\mathrm{s}$). Note that q, q_s, and V_h vary with the pressure (p), while IWV, IWV$_\mathrm{s}$, IVT, and IVT$_\mathrm{s}$ vary with the integration limit p_t.

The saturation IWV (IWV$_\mathrm{s}$) in Fig. 1b and the saturation IVT (IVT$_\mathrm{s}$) in Fig. 1c are obtained by replacing q in Eq. (1) with q_s, and they are given as functions of p_t that varies from p_b (1011 hPa) to 100 hPa, i.e.,

$$\mathrm{IWV_s}(p_\mathrm{t}) = \frac{1}{g}\int_{p_\mathrm{t}}^{p_\mathrm{b}} q_\mathrm{s}\mathrm{d}p, \quad \mathrm{IVT_s}(p_\mathrm{t}) = \frac{1}{g}\int_{p_\mathrm{t}}^{p_\mathrm{b}} q_\mathrm{s}|\mathbf{V}_\mathrm{h}|\mathrm{d}p. \tag{3}$$

Figure 1 shows that changing p_t from 300 hPa to 100 hPa has a negligibly small contribution to IWV or IVT, even with the assumption of a fully saturated layer (i.e., further increase in IWV$_\mathrm{s}$ or IVT$_\mathrm{s}$ as p_t becomes less than 300 hPa is also negligible). Therefore, for most operational applications, it is acceptable to set $p_\mathrm{t} = 300$ hPa in Eqs. (1) and (3). As a compromise between computational efficiency and accuracy in high-elevation areas (such as the Tibetan Plateau), we use $p_\mathrm{t} = 200$ hPa in this study. For non-operational applications, one can raise this level to 100 hPa (e.g., Rutz et al., 2014), which should be more appropriate in the tropical and subtropical areas, where intense convection may inject noticeable amounts of moisture into the upper troposphere (Zhu et al., 2000).

2.3 Column Relative Humidity as a Complement to AR Analysis

The IWV defined in Eq. (2) represents the total water vapor contained in a vertical air column of unit cross-sectional area. How much of this total water vapor content can condense and fall to the ground as precipitation depends of the degree of air saturation. In a simple cumulus parameterization scheme, Anthes (1977) used a vertical average of relative humidity (RH) to represent the degree of saturation of the air column. This measure gives equal weight to the upper and lower atmosphere. For an equal RH, however, the mass of water vapor in the lower atmosphere is much larger than that in the upper atmosphere. Therefore, to estimate the large-scale precipitation it is more appropriate to define a CRH as the ratio of IWV to $\mathrm{IWV_s}$ (e.g., Bretherton et al., 2004),

$$\mathrm{CRH} = \Re = \mathrm{IWV}/\mathrm{IWV_s}. \tag{4}$$

As shown in Fig. 1b, both IWV and $\mathrm{IWV_s}$ increase rapidly with height only in the lower atmosphere. The growth rate reduces to near zero above the 300-hPa level. Therefore, the CRH defined by Eq. (4) can be considered as a weighted average of RH favoring the lower atmosphere. For example, the CRH is 0.90 for the sounding shown in Fig. 1. If we set $q = 0$ for $p < 500$ hPa, the CRH is reduces slightly to 0.87. However, if we let $q = 0$ for $p > 500$ hPa, the CRH becomes 0.07, a much small value. Note that CRH can be readily derived from an atmospheric profile with temperature, dewpoint (or specific humidity), and pressure. A Python program for calculating IWV, IVT, and CRH is provided in the supporting information.

The CRH as a useful complement to the standard AR analysis is demonstrated in Fig. 2. It is shown that there were three frontal systems over the northeast Pacific Ocean at 1200 UTC 27 November 2020, and one of them was driving an AR onto the central coast of BC. Based on the IWV distribution, this AR could be categorized as an "Pineapple Express" storm for its apparent origin in the subtropical area near the Hawaiian Islands (Dettinger, 2004; Mo, 2016), However, the IWVF distribution (Fig. 2b) indicates that the moisture fluxes are towards rather than away from Hawaii. Therefore, the AR in question may represent the footprints left behind by a cyclone-anticyclone couplet that channeled moisture evaporating at local or nearby latitudes into a narrow band (e.g., Bao et al., 2006; Sodemann & Stohl, 2013; Dacre et al., 2015; Liu et al., 2016; Li et al., 2017). This AR can also be readily identified as a moist band in the CRH distribution (Fig. 2c). Note that to the northwest of this AR there was a frontal system associated with an oc-

cluded cyclone in the Gulf of Alaska. The values of IWV and IVT are relatively low around this system, so there is no AR associated with it. However, there is a band of high CRH along the cold front and into the low, which is co-located with a thin line of intense precipitation indicated by the forecast precipitation rate (FPR) distribution in Fig. 2d.

The IVT distribution in Fig. 2b suggests that the AR is in the weak to moderate category based on the scale proposed in Ralph et al. (2019). Nevertheless, the FPR distribution in Fig. 2d indicates intense precipitation in some coastal areas of BC. Some heavy precipitation events were indeed produced by this AR and they could be the trigger for a massive landslide in the Coast Mountains around 1400 UTC 28 November 2020 (Jones, 2021; Pollon, 2021). Massive rock and glacial ice fell into a glacial lake and then swept down stream as a large wave of wavter and debris destroying the densely forested Elliot Creek Valley downstream. The slide discharged large amounts of sediment and floating log hazards into the ocean at the head of Bute Inlet. A more detailed analysis of this case will be given in Section 4.

3 Water Balance Requirements in the Atmosphere

Since water cannot be created nor destroyed in the atmosphere, its local change can only occur through the addition or subtraction in any of its three possible phases (vapor, liquid, and solid), as described by the following balance equation (e.g., Peixoto, 1973, Eq. 14):

$$\frac{\mathrm{d}(q+q_\mathrm{c})}{\mathrm{d}t} = \left[\frac{\partial q}{\partial t} + \nabla\cdot(q\mathbf{V}_\mathrm{h}) + \frac{\partial(q\omega)}{\partial p}\right] + \left[\frac{\partial q_\mathrm{c}}{\partial t} + \nabla\cdot(q_\mathrm{c}\mathbf{V}_\mathrm{h}) + \frac{\partial(q_\mathrm{c}\omega_\mathrm{c})}{\partial p}\right] = 0, \qquad (5)$$

where $\nabla\cdot$ is the two-dimensional horizontal divergence operator, $\omega = \mathrm{d}p/\mathrm{d}t$ is the vertical velocity in the p coordinate system, ω_c is the averaged vertical velocity of the condensed water (liquid droplets or solid ice particles) relative to air.

For the total water balance, precipitation and evaporation at the Earth's surface must be considered. If the effects of climate change are ignored, over a long period of time the total water content in the atmosphere should not suffer any appreciable change, leaving the total global precipitation to be balanced by the corresponding evaporation in the hydrological cycle. Such a balance does not necessarily apply to a regional domain and over a synoptic timescale. For a persistent event of heavy precipitation, the horizontal transport of water vapor becomes a necessary condition.

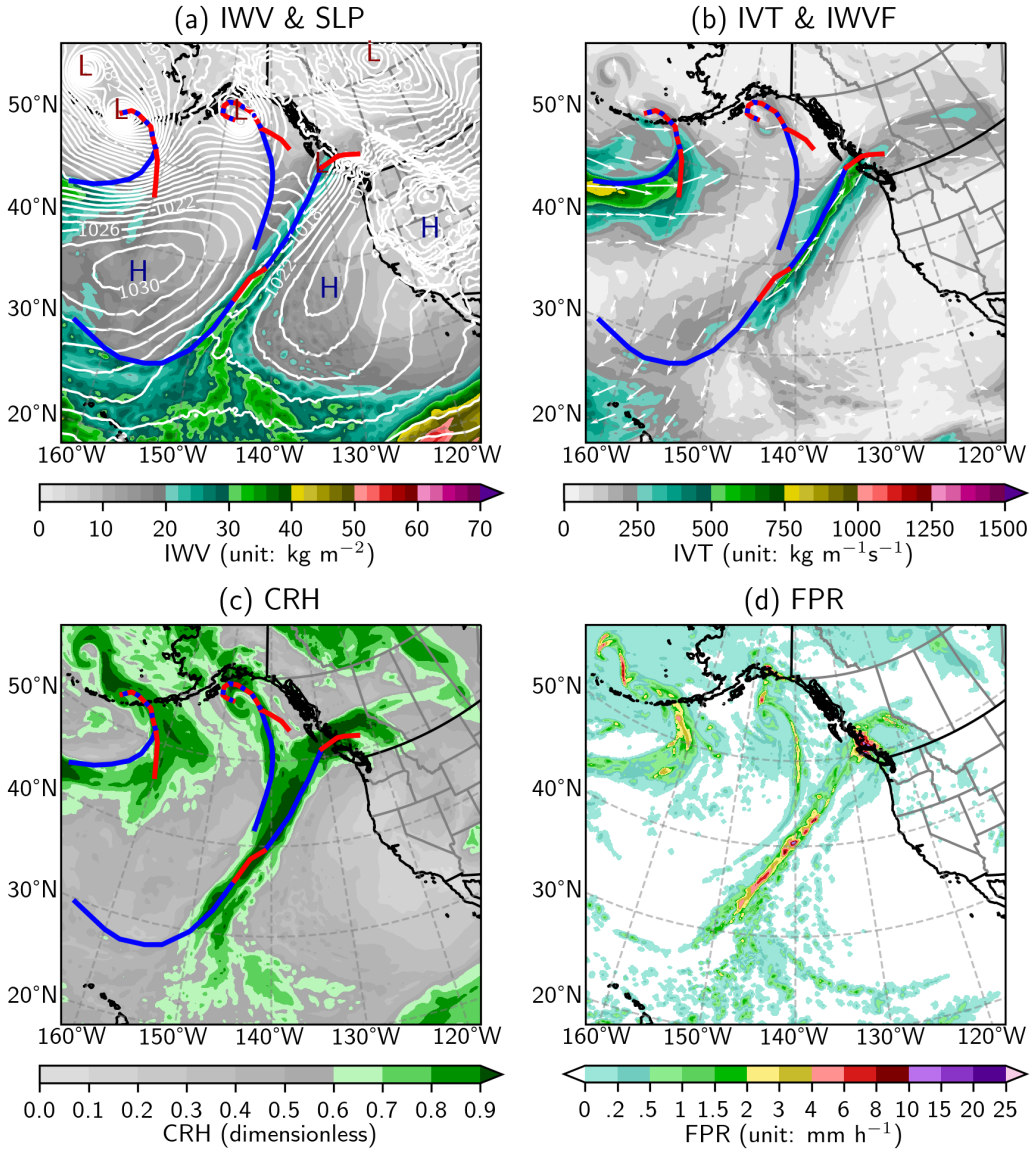

Figure 2. Atmospheric river conditions over the Northeast Pacific Ocean and the west coast of North America, valid at 1200 UTC 27 November 2020. (a) Sea level pressure (SLP, line contours, unit: hPa, intervals: 2 hPa; centers of low and high pressure are marked by L and H, respectively) and IWV (color-filled, unit: kg m^{-1}). (b) IVT (unit: kg m^{-1}s^{-1}) and normalized IWVF vectors, $\hat{\mathbf{Q}} = \mathbf{Q}/(|\mathbf{Q}| + 250\,\mathrm{kg\,m^{-1}s^{-1}})$. (c) CRH (dimensionless). (d) Forecast precipitation rate (FPR, unit: mm h^{-1}). In (a)–(c), all fields are based on the GDPS analysis (0-hour forecast fields); cold and warm fronts are represented by blue and red solid lines, respectively, and occluded fronts are marked by red-blue dashed lines. The FPR in (d) is the 24h lead-time prediction by the the GDPS run initialized at 1200 UTC 26 November 2020.

3.1 Water Balance Within an Air Column and Precipitation

Vertically integrating Eq. (5) from the bottom to the top of the atmosphere gives an equation that links precipitation and evaporation measured at the Earth's surface (boundary conditions) with the total water balance within an air column,

$$P = E - \frac{1}{\rho_{\mathrm{w}}}\left(\frac{\partial W}{\partial t} + \nabla \cdot \mathbf{Q}\right) - \frac{1}{\rho_{\mathrm{w}}}\left(\frac{\partial W_{\mathrm{c}}}{\partial t} + \nabla \cdot \mathbf{Q}_{\mathrm{c}}\right). \tag{6}$$

In the above equation, P and E are the rates of downward precipitation and upward evaporation, and $\rho_{\mathrm{w}} = 1000$ kg m^{-3} is the liquid water density. The quantities $\partial W/\partial t$ and $\partial W_{\mathrm{c}}/\partial t$ represent the rates of change in vapor phase and in condensed phase of water storage within the air column, respectively. The terms $\nabla\cdot\mathbf{Q}$ and $\nabla\cdot\mathbf{Q}_{\mathrm{c}}$ are the divergences of integrated water vapor flux and condensed water flux, respectively. The inclusion of ρ_{w} in this equation means that the unit for P and E can be conveniently chosen as m s^{-1}, mm h^{-1} or mm (24h)$^{-1}$.

The storage of water in the atmosphere in the vapor phase is much larger than that in the condensed phase, and the same applies to their local time rates of change, i.e., $\partial W/\partial t \gg \partial W_{\mathrm{c}}/\partial t$ (Peixoto, 1973). While the divergence of condensed water flux, $\nabla\cdot\mathbf{Q}_{\mathrm{c}}$, can at times be as important as the divergence of vapor flux, $\nabla\cdot\mathbf{Q}$ (Peixoto, 1973; Mo et al., 2019), its role in the precipitation process is often considered as secondary (Starr & Peixoto, 1958; Trenberth & Guillemot, 1998; Stohl & James, 2004; Cordeira et al., 2013; Mo & Lin, 2019). For a heavy precipitation event, the contribution from local evaporation is negligible, and the dominant factor is the net condensation rate (CR) represented by the second term on the right-hand side of Eq. (6),

$$\mathrm{CR} = -\frac{1}{\rho_{\mathrm{w}}}\left(\frac{\partial W}{\partial t} + \nabla \cdot \mathbf{Q}\right) = -\frac{1}{\rho_{\mathrm{w}}}\left[\left(\frac{\partial W}{\partial t}\right)_{\mathrm{p}} + \nabla \cdot \mathbf{Q} + \left(\frac{\partial W}{\partial t}\right)_{\mathrm{s}}\right] = \mathrm{PCR} + \mathrm{SCR}. \tag{7}$$

In the above equation, CR is further partitioned into a primary condensation rate, PCR $= -\rho_{\mathrm{w}}^{-1}[(\partial W/\partial t)_{\mathrm{p}} + \nabla\cdot\mathbf{Q}]$, which is attributed solely to the convergence of IWVF that results in general moistening and condensation, and a secondary condensation rate (SCR) due to other factors (e.g., radiative cooling and/or cold advection).

3.2 An Algorithm for Diagnosing the PCR Based on the CRH

The PCR in Eq. (7) can be parameterized into a non-negative, diagnosable variable,

$$\mathrm{PCR} = \begin{cases} -a\rho_{\mathrm{w}}^{-1}\nabla\cdot\mathbf{Q}, & \text{if } \nabla\cdot\mathbf{Q} < 0, \\ 0, & \text{if } \nabla\cdot\mathbf{Q} \geq 0, \end{cases} \tag{8}$$

with $0 \leq a \leq 1$. It is assumed that a fraction a of the total converged water vapor is condensed, while the remaining fraction $(1-a)$ is stored in the air to increase the humidity (Kuo, 1974). For an AR-induced heavy precipitation event, it may be safely assumed that PCR $\gg$ SCR and so the PCR should be the dominant factor on the right-hand side of Eq. (6), i.e., $P \approx \mathrm{PCR}$ (Mo et al., 2019; Mo & Lin, 2019).

For a fully saturated air column, any moisture convergence should be balanced by condensation, i.e., $a = 1$. In general, we can let a be a function of the CRH ($\Re$) in the following form (*cf.* Anthes, 1977)

$$a = \begin{cases} \left[(\Re - \Re_{\mathrm{c}})/(1-\Re_{\mathrm{c}})\right]^n, & \text{if } \Re > \Re_{\mathrm{c}}, \\ 0, & \text{if } \Re \leq \Re_{\mathrm{c}}, \end{cases} \tag{9}$$

where $\Re_{\mathrm{c}}$ and n are parameters that may be empirically adjusted. Note that Anthes (1977) used a similar formula in his cumulus parameterization scheme, i.e., $a = 1 - [(1-\langle\mathrm{RH}\rangle)/(1-\mathrm{RH_c})]^n$ if $\langle\mathrm{RH}\rangle \geq \mathrm{RH_c}$, otherwise $a = 0$. Here $\langle\mathrm{RH}\rangle$ is the mean relative humidity in the air column. As mentioned earlier, for AR analyses dealing with large-scale precipitation, CRH is better than $\langle\mathrm{RH}\rangle$ as a column saturation index, because it gives less weight to the upper atmosphere where the specific humidity is much lower than it is in the lower atmosphere (Fig. 1b). We have also tested Anthes' formula with $\langle\mathrm{RH}\rangle$ replaced by $\Re$. Its performance is not better than that of Eq. (9).

3.3 Optimal Parameters for the PCR algorithm

The FPR in Fig. 2d was derived from the GDPS operational forecast output. It was calculated based on a complicated scheme in the NWP model to simulate various thermodynamic processes, including deep, shallow, and elevated convection as well as large-scale clouds and precipitation (McTaggart-Cowan et al., 2019). To estimate the contribution from horizontal water vapor transport, we can calculate the PCR from Eq. (8) based on the forecast IVT and CRH fields and compare it with the FPR. As a first step, we can take the FPR as a reference to find the optimal values of n and $\Re_{\mathrm{c}}$ in Eq. (9).

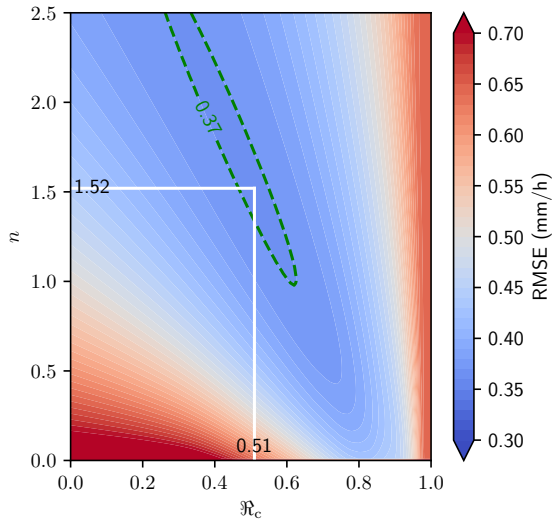

Figure 3. Global-average root mean-squared error (RMSE) between the FPR and the PCR based on the GDPS 24h lead time prediction, valid at 1200 UTC 27 November 2020. The minimum RMSE is located at $n = 1.52$ and $\Re_c = 0.51$.

Figure 3 shows the global-average root mean-squared error (RMSE) between the FPR and the corresponding 24h forecast PCR with n varying from 0 to 2.5 and $\Re_c$ from 0 to 1, valid at 1200 UTC 27 November 2020. The optimal parameters for Eq. (9) estimated from this case are $n = 1.52$ and $\Re_c = 0.51$.

To investigate the variability in this kind of parameter estimation, we use a full year of GDPS 24h forecast output (from 1 January to 31 December 2020, two runs a day) to create a 732-member ensemble and calculate the optimal parameters for each model run (Fig. 4). With all members included, the ensemble-mean optimal parameters for Eq. (9) are $n = 1.25 = 5/4$ and $\Re_c = 0.60$ (Fig. 4a). There is indeed some case-to-case variability due to either random effects or seasonal variation of atmospheric conditions (Fig. 4b vs. Fig. 4c). Nevertheless, the ensemble points are spread around a linear regression line relating the optimal $\Re_c$ to the specified n as follows

$$\Re_c = 0.826 - 0.177n. \tag{10}$$

For $n = 1$, this regression equation gives $\Re_c = 0.65$ as the optimal value. In a preliminary study with a different ensemble dataset (from 1 November 2019 to 31 October 2020), Mo (2020) let $n = 1$ and found that the best value for $\Re_c$ was 0.66.

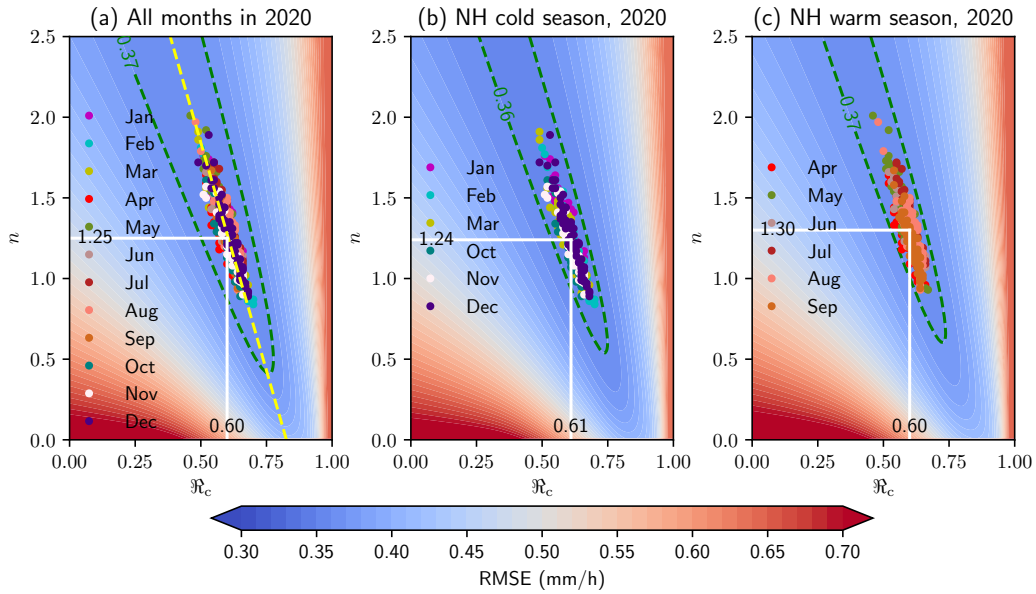

Figure 4. A full-year ensemble of global-average RMSE between the FPR and the PCR based on the GDPS 24h lead time prediction. The 732 ensemble members are from the GDPS twice-daily runs, initialized at 0000 and 1200 UTC respectively, from 1 January to 31 December 2020. The color-filled contour pattern represents the ensemble-mean global-average RMSE and the colored dots indicate the minimum RMSE of each ensemble member. (a) The plot for all months in 2020, with which the ensemble-mean minimum RMSE is located at $n = 1.25$ and $\Re_c = 0.60$; a regression equation obtained from these full-year ensemble data is $\Re_c = 0.826 - 0.177n$, which is indicated by the yellow dashed line. (b) The plot for the Northern Hemisphere (NH) cold-season months. (c) The plot for the NH warm-season months.

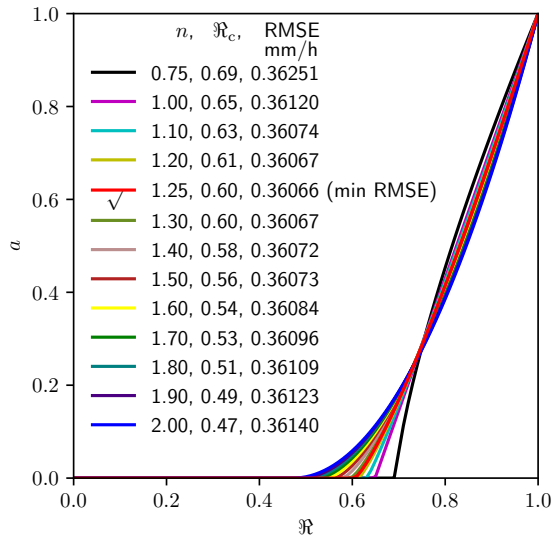

Figure 5. Variation of a defined in Eq. (9) as a function of $\Re$ for some selected parameters n and the optimal $\Re_c$ determined by the regression relation (10). The corresponding ensemble-mean RMSE (mm/h) in Fig. 4a is given in the embedded table.

Figure 5 shows the coefficient a as a function of $\Re$ in Eq. (9) for some selected n with the corresponding $\Re_c$ based on the regression relation (10). The embedded table also lists the ensemble-mean RMSE (Fig. 4a) for each pair of n and $\Re_c$. It shows that, for n ranging from 1.10 to 1.70, the algorithm achieves practically the same level of accuracy. Note that the coefficient a for each of the 13 selected pairs of parameters in Fig. 5 is either equal or very close to zero for $\Re < 0.50$, suggesting that the contribution of water vapor convergence to precipitation in the areas with $\Re < 0.50$ is generally negligible. Figure 5 also shows that especially for values of $\Re > 0.7$, given a specific $\Re$ the value of a does not change appreciably for any $\Re_c$ and n combination found along the minimum RMSE regression line. This suggests that for a given CRH a fairly specific amount of water vapor convergence must go to moistening the column rather than to precipitation. Unless stated otherwise, in this study we choose the ensemble-mean optimal parameters, $n = 5/4$ and $\Re_c = 0.60$, for Eq. (9). A Python program for calculating PCR is given in the supporting information.

4 Three Case Studies

In this section, we perform three case studies to demonstrate the usefulness of PCR and CRH as two supplements to standard AR analysis. The first case focuses on a cold-season AR affecting BC in late November 2020. A snapshot of this AR has been shown in Fig. 2. To highlight seasonal variations in AR characteristics (e.g., Guan & Waliser, 2019), we also examine two warm-season AR events in mid-August 2020 over East Asia and the northeast Pacific Ocean, respectively; these two events can also be seen in the global distributions of IWV, IVT, CRH, and PCR given in the supporting information (Figs. S1 and S2).

4.1 A cold-season AR in late November 2020

Figure 2 shows an AR affecting western Canada at 1200 UTC 27 November 2020. This AR was generated by a cyclone-anticyclone couplet over the northwest Pacific Ocean on the 23rd. As it moved into the northeast Pacific, the cyclone merged with the Aleutian Low in the Bering Sea and the anticyclone ran into the North Pacific High off the west coast of the United States. As shown in Fig. 6, the AR made landfall over the Alaska Panhandle around 0000 UTC on the 26th. In less than 24 hours, it moved to the central coast of BC and stalled there for about 18 hours (Fig. 6c,d and Fig. 2a,b). Throughout this period, the AR was driven mainly by the anticyclonic flow around the North Pacific High. A cyclonic wave began to develop at the northern edge of the AR around 0000 UTC on the 27th (Fig. 6c) and was located near the northern end of Vancouver Island at 1200 UTC (Fig. 2a). This cyclone could be considered as a reaction to latent heat release caused by the AR (e.g., Zhu & Newell, 1994). The AR lost its strength as it moved quickly across the south coast of BC in the afternoon of the 27th (Fig. 6e,f).

This AR produced locally heavy precipitation over the central and south coasts of BC as it moved across the region (Fig. 7). A BC Wildfire Service weather station (TS Effingham) on Vancouver Island received a total amount of 193.8 mm over a 48-hour period ending at 1200 UTC 28 November 2020. The maximum hourly amount of 13.6 mm at this station was observed at 0100 UTC on the 28th. The Machell station on the central coast received a total amount of 172 mm with a maximum hourly amount of 12.0 mm at 2100 UTC on the 27th. The precipitation intensity at Scar Creek was less impressive. It was in this region, however, a massive landslide from the Coast Mountains

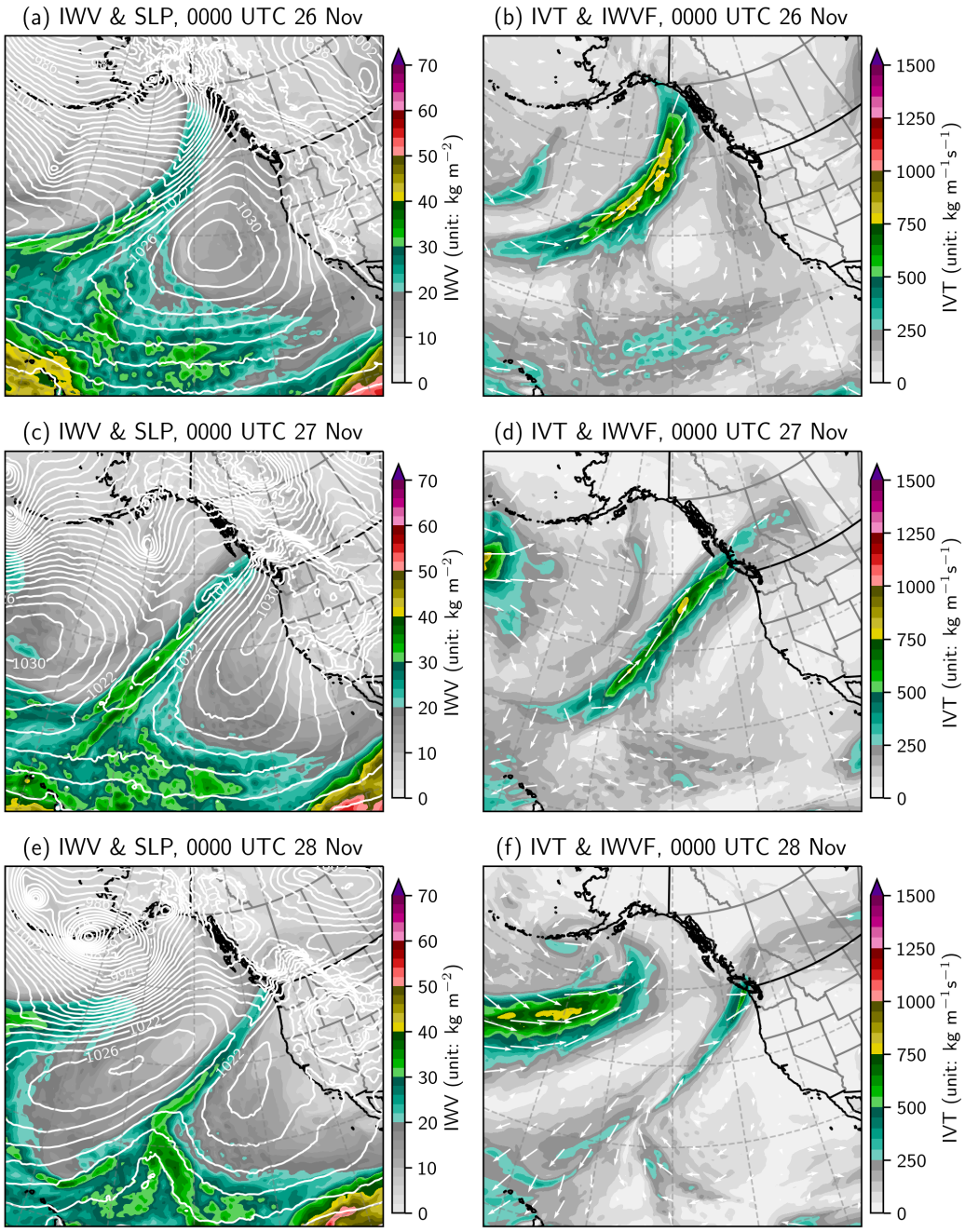

Figure 6. Atmospheric river conditions based on the GDPS analysis (0-hour forecast fields), valid at 0000 UTC 26–28 November 2020. The left panel shows the IWV (color-filled, unit: kg m^{-2}) and SLP (line contours, unit: hPa, intervals: 2 hPa). The right panel shows the IVT (color-filled, unit: kg m^{-1} s^{-1}) and normalized IWVF.

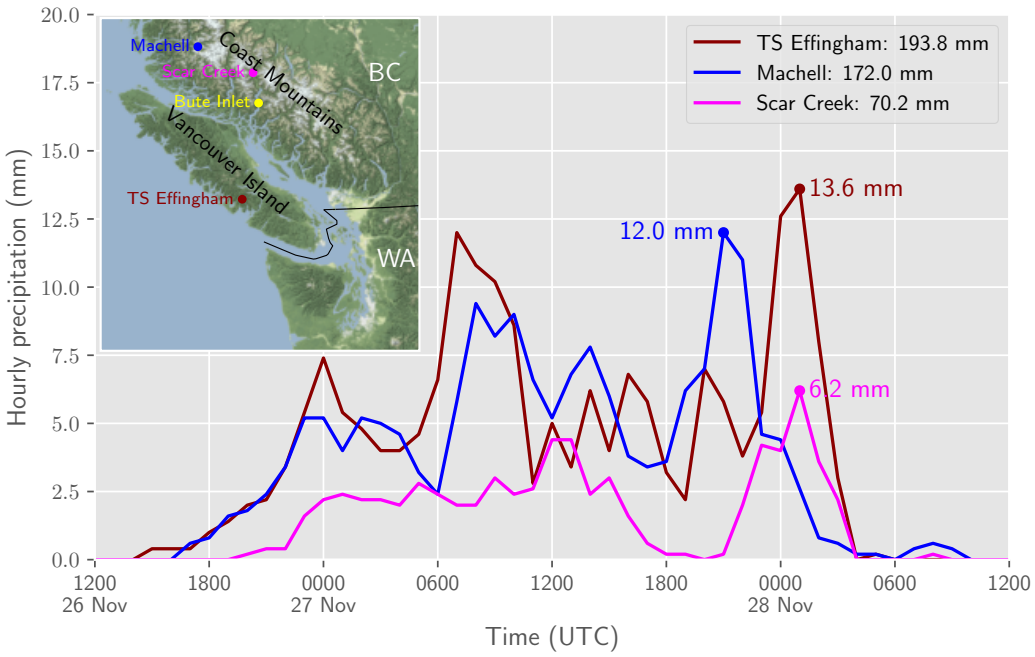

Figure 7. Hourly precipitation amounts observed at three weather stations of the BC Wildfire Service, TS Effingham, Machell, and Scar Creek, for an 48-hour period ending at 1200 UTC 28 November 2020. The storm-total amounts are given in the legend box. The station locations, together with the surrounding topographic features, are shown in an embedded map.

into Bute Inlet occurred around 1400 UTC on the 28th (Jones, 2021; Pollon, 2021). The AR-induced heavy precipitation could be one of the triggers for this geological disaster.

Figure 8 can be used for the comparison and verification purposes. Comparing Fig. 8a with Fig. 8b indicates that the area of heavy precipitation forecast for coastal BC is well captured in the forecast PCR field. The most intensive precipitation was forecast for West Vancouver Island, where the maximum FPR is between 15 and 20 mm h^{-1}. The forecast PCR in this region is less intense with a maximum value between 10 and 15 mm h^{-1}. In the central coast of BC, the maximum FPR (8–10 mm h^{-1}) is also more intense than the PCR (4–6 mm h^{-1}). These differences are understandable because the PCR is a diagnosed variable that is incapable of simulating sub-grid-scale convection. In addition, some of these differences could be attributed to the secondary condensation rate or other factors included in equations (6) and (7), such as cloud drift and local evaporation.

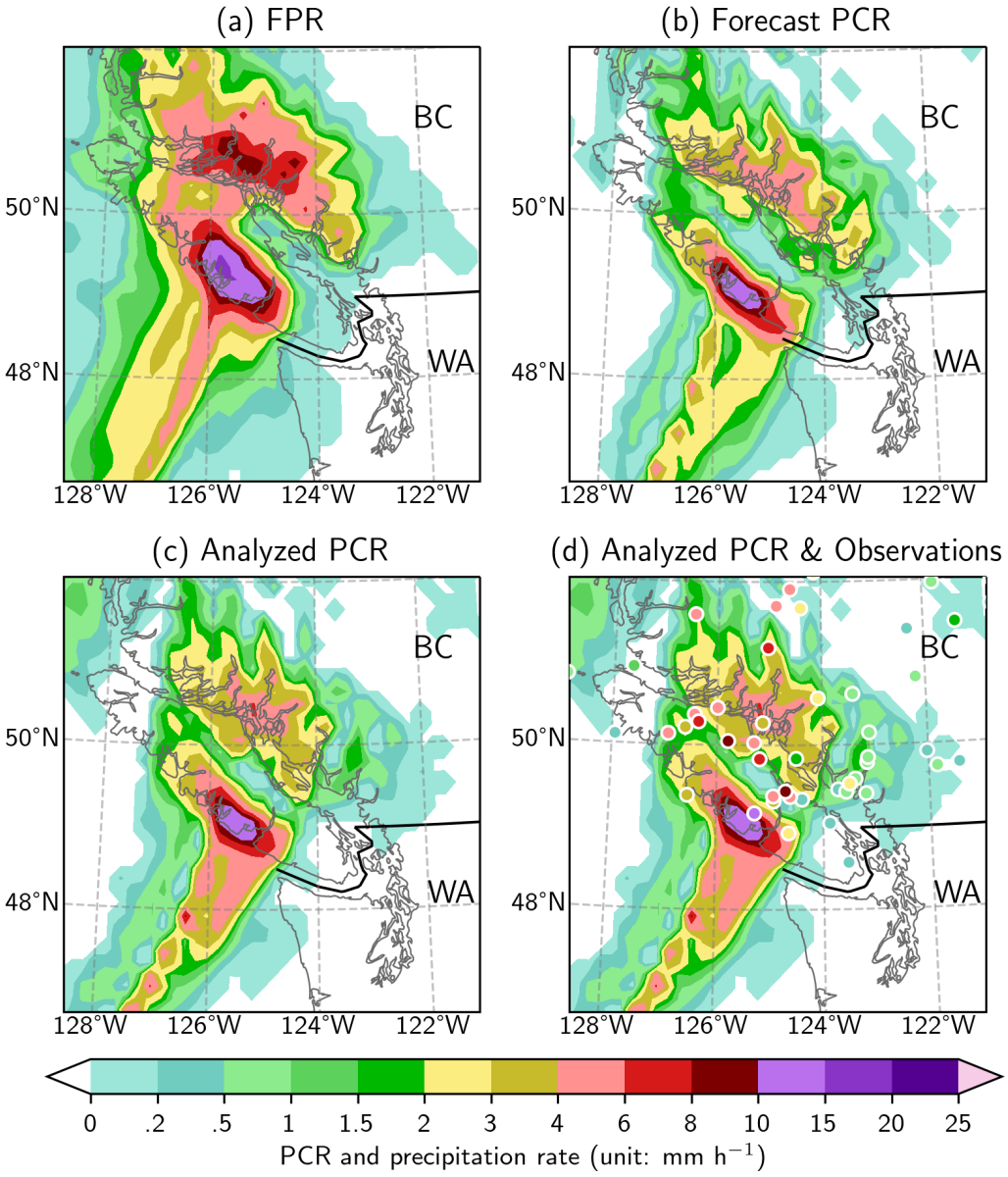

Figure 8. Atmospheric river analysis valid at 0000 UTC 28 November 2020. (a) The 24h lead-time forecast precipitation rate (FPR) from the operational GDPS run initialized at 0000 UTC on the 27th. (b) The PCR diagnosed from the 24h lead-time forecast fields. (c) The PCR based on the GDPS analysis (initial conditions) at 0000 UTC on the 28th. (d) The same PCR (color-filled) as in (c) and the maximum hourly precipitation amounts observed at weather stations valid at 0000 or 0100 UTC on the 28th (color dots).

It should be emphasized that the PCR is not designed to be an alternative to the FPR for operational forecast practice. Operational meteorologists need to analyze the FPR field for their quantitative precipitation forecast (QPF). PCR can help forecasters better quantify the contribution from the horizontal water vapor transport (AR) to the QPFs. When the QPF tools are not available, such as in some post-storm case studies or storm classification schemes, the diagnosable PCR can serve as a proxy for precipitation rate in AR analyses. The following example illustrates the use of PCR for ad hoc model verification and precipitation diagnosis.

Comparing Fig. 8b with Fig. 8c shows that the PCR from the 24h lead-time forecast verifies well against the analyzed PCR. The PCR pattern is also quite consistent with the hourly observations in Fig. 8d. As shown in Fig. 7, the maximum hourly amounts observed between 0000-0100 UTC 28 November at TS Effingham, Machell, and Scar Creek are 13.6, 4.4, and 6.2 mm, respectively. The corresponding PCR values in Fig. 8c are in the ranges of 10–15, 1.5–3, and 3–4 mm h^{-1}, repsectively. Some differences between the analyzed PCR and observed hourly amounts could be attributed to the spillover effect caused by the $\nabla \cdot \mathbf{Q}_c$ term in Eq. (6). Note that the hydrometeor drift downwind, especially for snow, is not simulated by the GDPS precipitation scheme; see relevant case studies on the BC south coast in Mo et al. (2019).

4.2 A Warm-Season AR Affecting East Asia

Heavy monsoonal rainfall ravaged a large swath of East Asia in summer 2020, leading to record-breaking flooding with devastating socioeconomic impacts (Zhang et al., 2021; Zhou et al., 2021). Here we focus on one AR event affecting this region in mid-August. The AR analysis valid at 0000 UTC 15 August 2020 is shown in Fig. 9. The IVT distribution indicates an AR moving across the Indochinese Peninsula, mainland China, the Korean Peninsula, and Japan. The major driving forces behind this AR include 1) the subtropical high pressure system in the northwest Pacific Ocean that forced the monsoonal flow to change direction and penetrate through the mainland of China (e.g., Chen et al., 2020); 2) the high plateau in western China that often acts as an orographic barrier, which intercepts and guides the tropical moist flow northwards through China (Lu, 1947); 3) a cold front associated with an occluded cyclone centered at (50°N, 128°E), which dragged the moist flow further into the extratropical North Pacific. This AR system started to form over eastern China on 12 August and lasted for more than four days

with severe hydrometeorological impacts. It produced numerous heavy precipitation events across areas from southwestern to northern China, and the rain-induced floods for the following few days devastated the Yangtze Basin and caused the worst flood-related damages ever seen in Chongqing, a megacity in Southwest China (Huang, 2020; Shih, 2020; Tan & Li, 2020).

Figure 9b shows that the IWV values are very high over tropical and subtropical areas, and because of this it is difficult to identify the AR over East Asia in terms of IWV with the color scheme tuned for the cold-season ARs in the extratropical regions. To match the southern (northern) boundary of the AR in Fig. 9a, one would need to mute the IWV values < 50 (< 30) kg m^{-2} with gray colors in Fig. 9b. One the other hand, the CRH distribution in Fig. 9c can be taken as a useful supplement to standard AR maps to help focus attention on the moist areas where precipitation efficiency is high. The AR is much easier to identify here than in Fig. 9b. Comparing Fig. 9c with Fig. 9a shows that bands of large CRH are not always co-located with bands of strong IVT. For example, the CRH-AR over China is shifted further north of the IVT-AR.

The PCR distribution in Fig. 9d shows a narrow band of heavy precipitation over China, which is co-located with the band of maximum CHR in Fig. 9c and slightly shifted to the north of the maximum IVT in Fig. 9a. Zheng et al. (2021) have pointed out that the heaviest precipitation is often located over the northeastern leading edge, northern boundary, or near the core of an AR object identified in the IVT distribution over the northeast Pacific Ocean. The PCR distribution in Fig. 9d is in good agreement with their observation. The areas with large PCR values are also consistent with the weather radar echo pattern shown in Fig. 10. This implies that most of the heavy precipitation can be attributed to the large-scale horizontal moisture convergence associated with the AR transport.

4.3 A Warm-Season AR Affecting Western North America

There was also an AR developing over the northeast Pacific Ocean in mid-August 2020. An analysis of this system valid at 0000 UTC 15 August 2020 is shown in Fig. 11. Both of the IVT and CRH distributions indicate a well-defined AR that just made landfall on the west coast of Canada. However, the southern boundary of the AR is poorly defined in terms of IWV with the chosen color scheme in Fig. 11b. Note that this AR

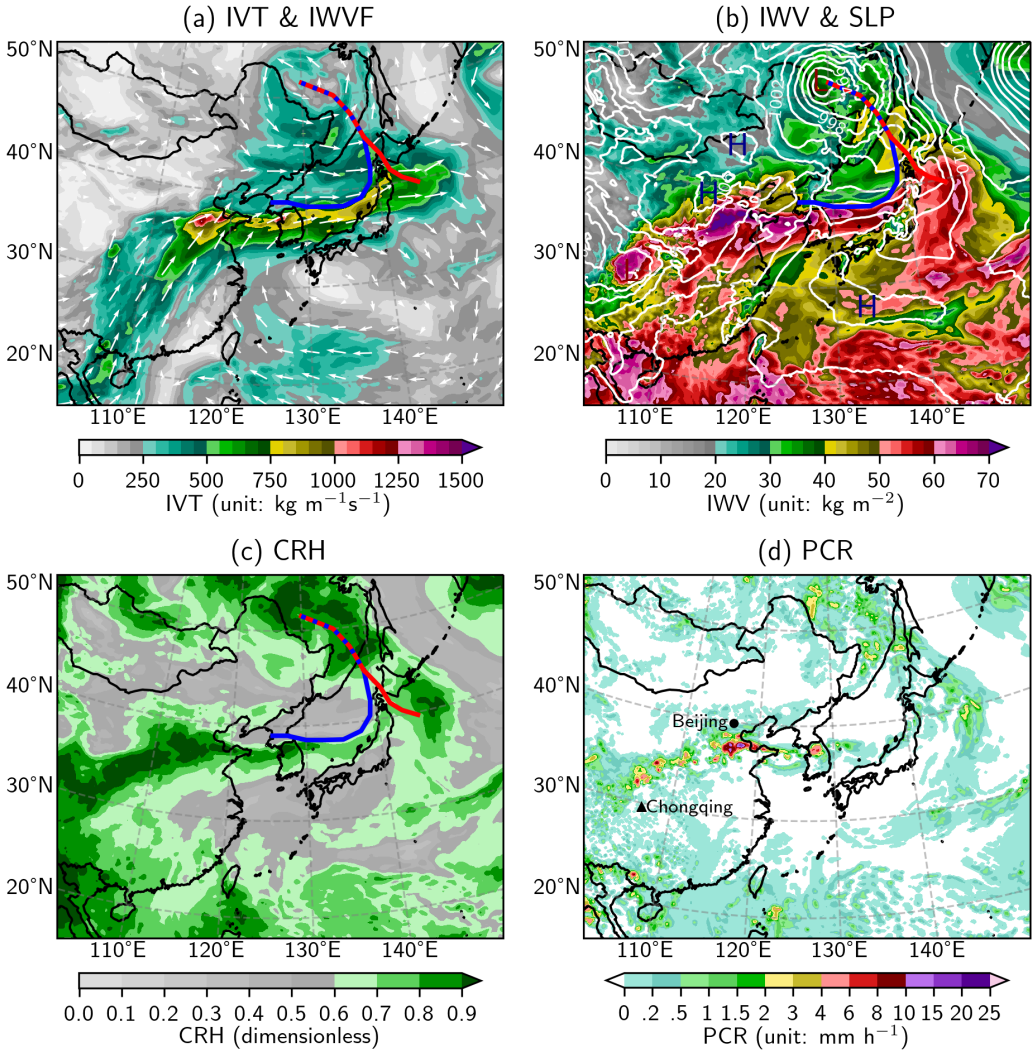

Figure 9. Atmospheric river and frontal analyses in East Asia valid at 0000 UTC 15 August 2020. All fields are from the GDPS analysis (0-hour forecast). (a) IVT (color-filled, unit: kg m^{-1}s^{-1}) and normalized IWVF (white vectors). (b) IWV (color-filled, unit: kg m^{-2}) and SLP (white solid contours, unit: hPa, intervals: 2 hPa). (c) CRH (dimensionless). (d) PCR (unit: mm h^{-1}).

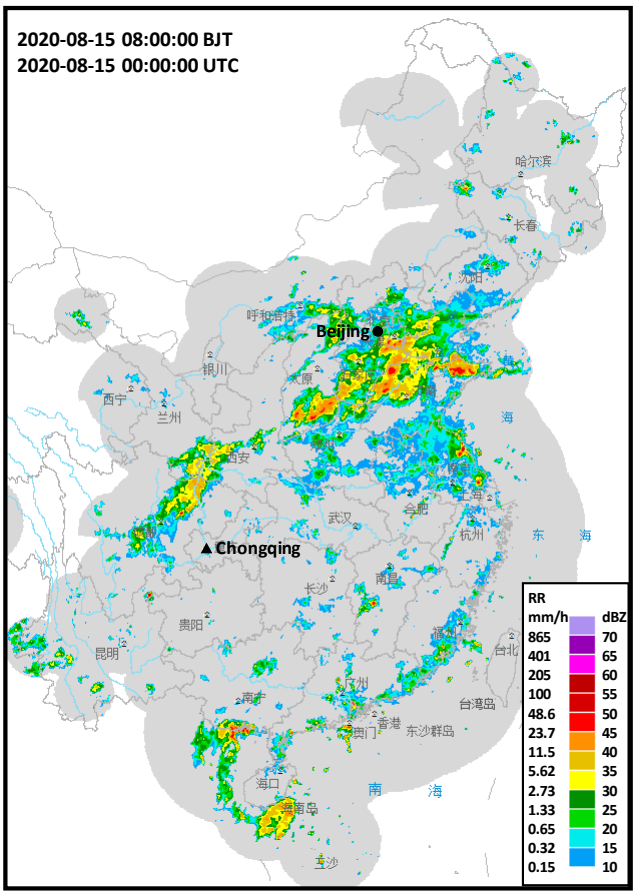

Figure 10. A radar mosaic valid at 0000 UTC 15 August 2020, obtained from `http://en.weather.com.cn/radar/`. The reflectivity decibels (dBZ) are converted to rain rate (RR) using the Marshall-Palmer formula: $\mathrm{RR} = [10^{(\mathrm{dBZ}/10)}/200]^{5/8}$ (Marshall & Palmer, 1948).

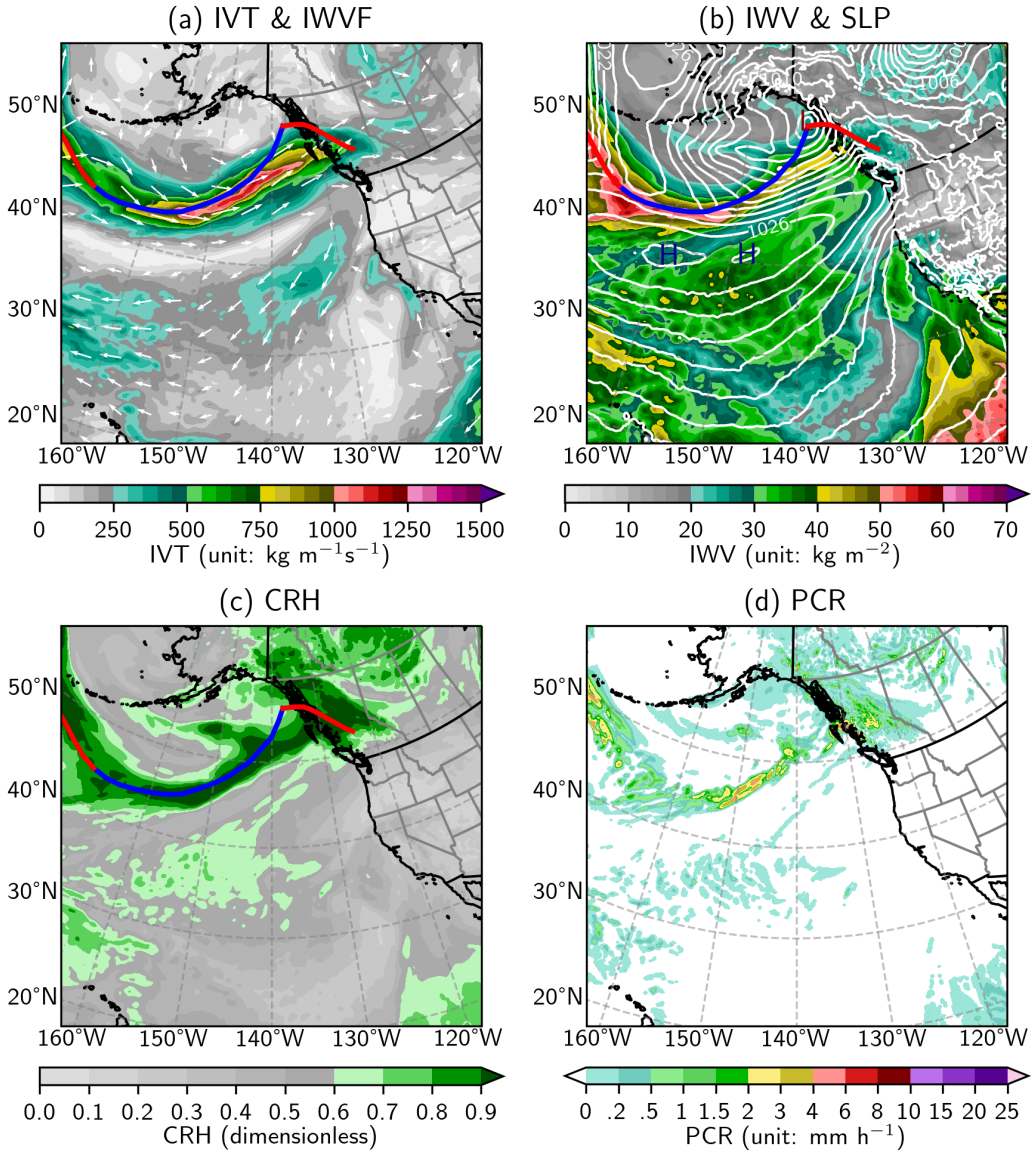

Figure 11. Same as Figure 9, except for the northeast Pacific Ocean and western North America.

made landfall around 0600 UTC 14 August. It was jointly driven by a mobile cyclone over the Gulf of Alaska and a quasi-stationary anticyclone to the south. It triggered locally heavy rainfall over the north and central coast of BC and caused a few landslides near the city of Prince Rupert (Millar, 2020). The 60h storm-total precipitation amount at the Prince Rupert Airport was 138 mm. The warm front also spread some rainfall into the BC interior.

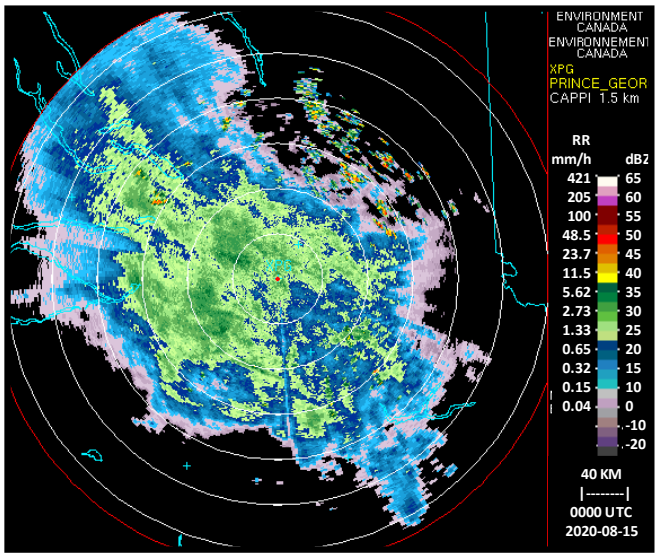

Figure 12. Echos on the 1.5-km CAPPI (Constant Altitude Plan Position Indicator) of the Prince George radar (CXPG: 53.61°N, 122.59°W), valid at 0000 UTC 15 August 2020. The reflectivity decibels (dBZ) are converted to rain rate (RR) using the Marshall-Palmer formula: $\mathrm{RR} = [10^{(\mathrm{dBZ}/10)}/200]^{5/8}$ (Marshall & Palmer, 1948).

The PCR distribution in Fig. 11d suggests heavy precipitation on the north and central coast of BC, where the onshore moist flow of the Pacific AR was intercepted by the Coast Mountains. It can be compared with the echo pattern of the Prince George radar (CXPG: 53:61°N, 122:59°W) in Fig. 12; there was no weather radar coverage for the rainy area on the coast. For a better comparison, we also plot the PCR distribution and the observed hourly precipitation amounts in a smaller domain in Fig. 13. The large PCR values over the central coast of BC are confirmed by observations at two stations, which reported hourly amounts from 8 to 10 mm. Over the BC north coast, the difference between the analyzed PCR and observed hourly rainfall amounts could be attributed to the spillover effect represented by the $\nabla\cdot\mathbf{Q}_c$ term in Eq. (6) (e.g., Mo et al., 2019). Ahead of the warm front in the central interior of BC, the PCR pattern is close to the hourly observations in Fig. 13b.

5 A Potential Application to the AR Classification

It was illustrated above that the PCR and CRH are useful supplements to routine AR analysis. A potential application of PCR to AR scaling is explored in this section.

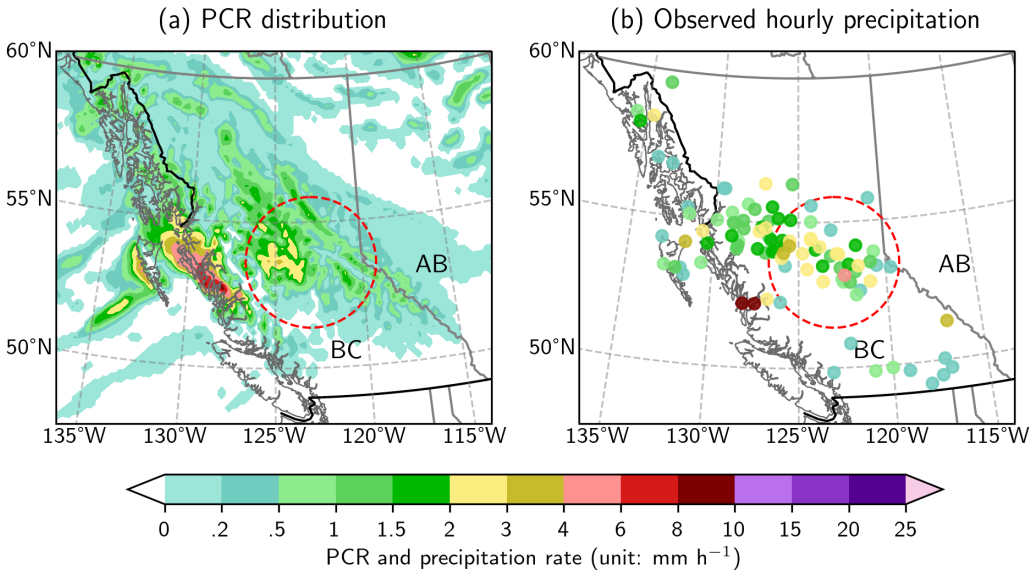

Figure 13. (a) The PCR distribution as in Fig. 11d, but in a smaller domain centered on British Columbia, Canada. (b) The maximum hourly precipitation amounts at weather stations valid between 0000 and 0100 UTC 15 August 2020. The red-dashed circle corresponds to the 250-km range of the Prince George radar in Fig. 12.

Ralph et al. (2019) have recently introduced a scale for AR analysis. This five-category scale is based on the IVT intensity and duration thresholds over a location, assuming that the AR impacts are proportional to the AR strength. It can be used to characterize AR strength and potential impacts in a simple way that is both useful to scientists and conducive to communication with non-experts. In this scaling system, the AR impacts are implied, but not directly quantified. It is desirable and possible to add an impact component to this system based on the mean precipitation rate (MPR), which can be calculated as either the storm-total precipitation amount devided by the storm duration, or the average of the model FPR or the diagnosable PCR. Table 1 and Fig. 14 outline a possible combined scale given in the format of ARx-Py, where "ARx" stands for the AR scale based on the IVT method of Ralph et al. (2019) and "Py" represents the precipitation impact component. Thus, if an AR moves across a location with a duration of 40h and a maximum IVT of 800 kg m^{-1}s^{-1}, it is categorized as an AR3 based on its strength. If the predicted or analyzed MPR over this 40h period is 120 mm (24h)$^{-1}$, it is classified as a P4 storm based on its precipitation impact. Therefore, the combined scale for this AR at this location can be given as AR3-P4. It should be emphasized that

there is no implication of a one-to-one correspondence between these two scales in Fig. 14. The AR-scale is based on the maximum IVT on the left chart, and the P-scale is based on the MPR on the right chart. They are quasi-independent, given that the MPR is calculated from FPR or PCR over the AR duration determined by IVT threshold (IVT $\geq$ 250 kg m^{-1}s^{-1}). An independent precipitation impact scale ($\tilde{\text{P}}$-scale) is also defined in Table 1 and Fig. 14.

Table 1. Top: the AR strength scale from Ralph et al. (2019) based on maximum instantaneous IVT magnitude and duration of AR conditions (i.e., IVT $\geq$ 250 kg m^{-1}s^{-1}). Bottom: a precipitation impact scale based on mean precipitation rate (MPR) and duration of AR conditions (P-scale) or $\text{P}_{6\text{h}}$ conditions ($\tilde{\text{P}}$-scale), where $\text{P}_{6\text{h}}$ is the past 6-hour total precipitation amount at synoptic hour: 0000, 0600, 1200, or 1800 UTC.

Max IVT	Duration (h) of AR conditions (IVT $\geq$ 250 kg m^{-1}s^{-1})		
(kg m^{-1}s^{-1})	$\leq$ 24	$\geq$ 24–48	$\geq$ 48
$<$ 250	Not an AR	Not an AR	Not an AR
$\geq$ 250–500	Negligible AR (AR0)	Weak AR (AR1)	Moderate AR (AR2)
$\geq$ 500–750	Weak AR (AR1)	Moderate AR (AR2)	Strong AR (AR3)
$\geq$ 750–1000	Moderate AR (AR2)	Strong AR (AR3)	Extreme AR (AR4)
$\geq$ 1000–1250	Strong AR (AR3)	Extreme AR (AR4)	Exceptional AR (AR5)
$\geq$ 1250	Extreme AR (AR4)	Exceptional AR (AR5)	Exceptional AR (AR5)

MPR	Duration (h) of AR conditions (IVT $\geq$ 250 kg m^{-1}s^{-1}): P-scale		
(mm/24h)	Duration (h) of $\text{P}_{6\text{h}}$ conditions ($\text{P}_{6\text{h}} > 1$ mm): $\tilde{\text{P}}$-scale		
	$\leq$ 24	$\geq$ 24–48	$\geq$ 48
$<$ 25	Negligible impact (P0)	Negligible impact (P0)	Negligible impact (P0)
$\geq$ 25–50	Marginal impact (P0)	Weak impact (P1)	Moderate impact (P2)
$\geq$ 50–75	Weak impact (P1)	Moderate impact (P2)	Strong impact (P3)
$\geq$ 75–100	Moderate impact (P2)	Strong impact (P3)	Extreme impact (P4)
$\geq$ 100–150	Strong impact (P3)	Extreme impact (P4)	Exceptional impact (P5)
$\geq$ 150	Extreme impact (P4)	Exceptional impact (P5)	Exceptional impact (P5)

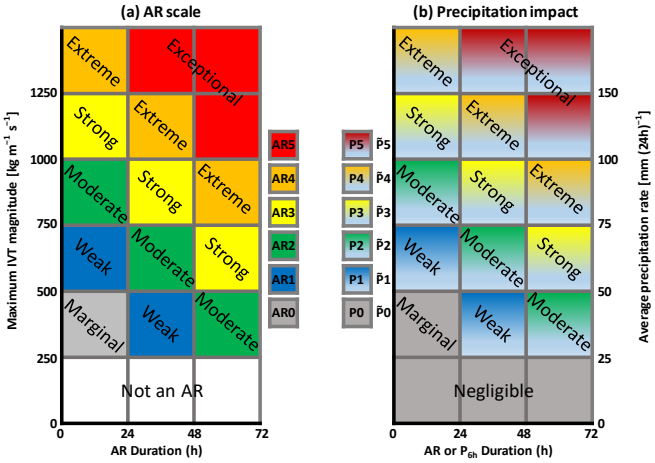

Figure 14. (a) An AR scale adopted from Ralph et al. (2019) that categorizes AR events based on the IVT conditions (IVT $\geq$ 250 kg m^{-1}s^{-1}). (b) A precipitation impact scale based on the mean precipitation rate (MPR) over a period of IVT conditions (IVT $\geq$ 250 kg m^{-1}s^{-1}, P-scale) or of P_{6h} conditions (P_{6h} > 1 mm), where P_{6h} is the past 6-hour total precipitation amount at synoptic hour (0000, 0600, 1200, or 1800 UTC). A combined scale can be given in the format of ARx-Py, where "ARx" is the AR-scale determined from (a), and "Py" is the P-scale determined from (b); these two components are calculated independently over the same duration of AR conditions.

Figure 15 shows an image from an experimental web-based application which utilizes the above-mentioned combined scale applied to the mid-August AR at selected locations in western Canada. is based on the GDPS prediction initialized at 0000 UTC 13 August 2020. The color-coded dots on the zoomable map indicate the predicted AR scale value (AR-scale) for the corresponding weather stations, and clicking on a station will present the user with two time series of IVT and FPR; the IVT-based AR duration is color-filled based on the corresponding AR-scale and P-scale. In this example, the MPR values calculated from the FPR and the PCR are indicated by the black dashed line and the red dotted line, respectively. The predicted strength and duration of this AR at Sandspit are similar to those at Prince Rupert, as illustrated in the IVT time series. However, the AR impacts on precipitation at these two stations are quite different; the stronger orographic forcing near Prince Rupert led to much heavier rainfall as suggested by the FPR time series. The MPR calculated from FPR (or PCR) at Sandspit over the 66h storm period is 7.3 (9.7) mm $(24\text{h})^{-1}$, as compared to 56.0 (57.4) mm $(24\text{h})^{-1}$ at Prince Rupert. Therefore, it would be appropriate to call this storm as an extreme AR with negligible impact (AR4-P0) at Sandspit, and an extreme AR with strong impact (AR4-P3) at Prince Rupert.

Our verification indicates that the GDPS model underforecast precipitation at Sandspit. The observed amount at this station is 41 mm over the 66h period ending at 0000 UTC 17 August, which is equivalent to an MPR of 14.9 mm $(24\text{h})^{-1}$ (double the predicted value). Nevertheless, it is still verified as an AR4-P0 or $\tilde{\text{P}}0$ storm. On the other hand, the forecast for Prince Rupert verified well. The observed amount at this station was 138 mm over the 60h ending at 1800 UTC 16 August, which translates into an MPR of 55.2 mm $(24\text{h})^{-1}$. It is therefore an AR4-P3 or $\tilde{\text{P}}3$ storm. The torrential downpours caused flash flooding and landslides in the Prince Rupert area, leaving mud, silt, and debris on some highway sections; a landslide that occurred about 42 km east of the city on 16 August forced the emergency evacuation of at least 13 people (Millar, 2020).

It should be emphasized that this simple scale may work well along the coastal areas, but would not apply to inland regions where such MPRs cannot be achieved. It might be possible to adjust the MPR criteria for specific areas based on local hydro-climatic conditions, or replace the MPR criteria with something else (e.g., the return period of precipitation intensity). In addition, the phase of precipitation can also be important. For instance, impacts of a 50 mm (water equivalent) snowfall or mixed precipitation over

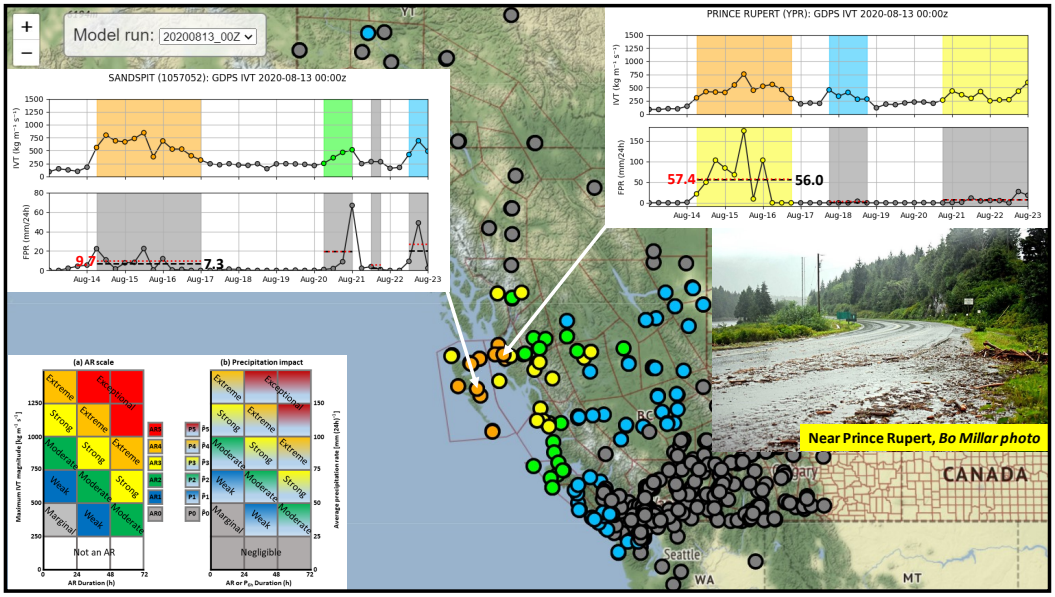

Figure 15. The predicted strength and impact scales of a mid-August AR over western Canada based on the GDPS operational forecast initialized at 0000 UTC 13 August 2020 and the proposal outlined in Table 1. The color of the dots on the map represents the AR scale from Ralph et al. (2019). The time series in the left panel show the IVT and FPR variations at Sandspit; the highlighted areas indicate the AR durations, and the area colors represent the AR scale (top) and precipitation scale (bottom), respectively. The time series in the right panel are for Prince Rupert. The values of mean precipitation rate (MPR) calculated from the FPR and the PCR for each AR duration are indicated by the black dashed and red dotted lines, respectively. The embedded photo (courtesy of Bo Millar) shows dangerous road conditions near Prince Rupert after torrential rain caused flash flooding in the area (Millar, 2020).

24 hours may be much more impactful to socio-economic activity than a similar amount of rainfall. Likewise, a succession of ARs of moderate intensity could have a cumulative effect on soil moisture, streamflow generation and hence the potential for floods. Considering all these factors is beyond the scope of this study.

As shown in Fig. 15, the MPR values calculated from the FPR and PCR are very close; for the two examples, the PCR-based values are slightly higher than the FPR-based values. From an operational meteorologist's perspective, it may not be necessary to analyze the PCR, given that the FPR is almost always available in a modern operational weather forecast environment. Nevertheless, analyzing the PCR distribution can help forecasters better understand the contribution of horizontal water vapor convergence to heavy precipitation. In some scientific studies, when precipitation rate is not available or not well calibrated in the dataset, PCR could be used as a proxy for estimated precipitation rate in storm classification analysis.

For the case on 27 November 2020 over the central and south coasts of BC, the operational GDPS forecast initialized at 1200 UTC on the 26th categorizes the AR at TS Effingham, Machell, and Scar Creek (see Fig. 7 for geo-references) as AR1-P2, AR0-P3, and AR0-P1, respectively (figures not shown). The maximum IVT at TS Effingham was less than 750 kg $m^{-1}s^{-1}$, and less than 500 kg $m^{-1}s^{-1}$ at the other two stations. The durations of this AR at these three stations were all less than 24 hours. On the other hand, based on the observed hourly precipitation amounts shown in Fig. 7, the independent precipitation impact scales at TS Effingham, Machell, and Scar Creek should be $\tilde{P}4$ (MPR = 111 mm/24h for 42h), $\tilde{P}3$ (MPR = 86 mm/24h for 48h), and $\tilde{P}1$ (MPR = 47 mm/24h for 36h), respectively.

6 Discussion and Conclusions

Precipitation is one of the most important weather elements, but forecasting it can be difficult because it varies widely in time and space. The development of heavy and prolonged precipitation requires a sufficient supply of moisture and a physical mechanism to produce condensation. Atmospheric rivers, defined as long and narrow corridors of strong horizontal moisture transport, can provide such necessary conditions. A standard AR analysis usually involves calculating the IWV and IVT to identify the strength, location, and movement of the AR system. In this study, we propose the column rela-

tive humidity and the primary condensation rate as two supplements to the standard AR analysis to focus attention on the AR contribution to heavy precipitation. Both CRH and PCR are diagnosable variables. The CRH measures the relative moistness of the air column and the PCR can be used as a proxy measure of the large-scale precipitation rate.

The PCR is defined as a simple function of the CRH and the convergence of integrated horizontal water vapor flux. It is based on the concept that the converged vapor is shared between condensation and a general moistening of the air column. There are two empirically adjustable parameters in our proposed algorithm for PCR. Their optimal values were determined in this study based on a full year of NWP model data. Our case studies showed that the diagnosed PCR can be used to correctly identify the location and amount of heavy precipitation associated with ARs. The location of heavy precipitation is not necessarily co-located with the maximum IVT, because precipitation is directly associated with the net convergence rather than with the transfer of moisture. The moisture convergence in the lower atmosphere can be caused by orographic or frontal forcing, which usually also includes the physical mechanism to set up the vertical motions necessary to produce condensation and precipitation. In a recent study, Zheng et al. (2021) analyzed the detailed IVT distributions of 15 ARs using conventional observations and reconnaissance data from a targeted field campaign over the Northeast Pacific. They showed that the heaviest precipitation often occurs in the core, northeastern boundary, and the leading edge of an AR. This is not surprising because these locations are the most prone to strong horizontal convergence.

The precipitation efficiency also depends on the initial vertical distribution of water vapor in the air column, which is indicated by the CRH, and it can be expected that heavy precipitation is always associated with a large value of CRH. Our case studies showed that precipitation in the areas with CRH < 0.5 is negligible. In this study, the cut-off value of CRH for the PCR algorithm is 0.6. Our case studies also indicated that the equatorward boundary of ARs can be more clearly defined by the CRH than the IWV, especially in the warm seasons when IWV values are very large in tropical and subtropical regions.

The diagnosable PCR focuses attention on the primary factor leading to condensation: the horizontal water vapor transport and convergence. It can be used to represent the primary precipitation rate (PPR) if, and only if, condensed water storage is neg-

ligible. Note that in Eq. (6) the divergence of condensed water flux, $\nabla \cdot \mathbf{Q}_c$, can be at times as important as the convergence of vapor flux, $-\nabla \cdot \mathbf{Q}$. Under such circumstances, one can define PPR = (PCR $- \rho_w^{-1} \nabla \cdot \mathbf{Q}_c$) ≥ 0. This is usually the case when an AR is blocked by a large mountain range. A fraction of the condensation over the windward slope will be carried by strong winds to the leeward side of the mountain, leading to the spillover phenomenon (e.g., Mo et al., 2019). To deal with this issue, one needs to estimate the vertical distribution of the specific condensed water q_c. This is sometimes challenging because it is much more difficult to measure q_c than q in the atmosphere, and some NWP model data (including reanalyses) only have q_c for cloud condensates.

In an operational forecast environment, the quantitative precipitation forecasts should be based on the FPR provided by the NWP model guidance rather than the less-accurate PCR. The added value of PCR is to help operational forecasters better understand the contribution of horizontal water vapor convergence to heavy precipitation. A potential application of PCR or FPR in storm classification analysis is also discussed in this study. It is possible to add an impact component to the AR scale introduced by Ralph et al. (2019), so that an AR could be categorized using a combined scale in the format of "ARx-Py", where "ARx" is the AR scale based on its strength and duration (Ralph et al., 2019), and "Py" is the scale based on its precipitation impact calculated from the time average or integration of PCR or FPR. From a user perspective, a storm scale has to be simple enough that there is no confusion when an impact-based forecast is communicated to the general public and decision makers. The AR scale introduced by Ralph et al. (2019) uses the intensity of IVT and event duration to characterize AR strength. It is simple and straightforward. When it is used as a proxy for estimated impact, the underlying assumption is that the IVT and the resulting precipitation rate are linearly correlated. Since precipitation is directly associated with the net moisture convergence rather than with the IVT, it would be useful, and perhaps necessary, to add a component such as the P-scale to explicitly address the AR impact on precipitation. An independent precipitation impact scale ($\tilde{\text{P}}$-scale) is also defined in Table 1 and Fig. 14b.

It is also possible to develop a multi-impact scale that includes several more hydroclimatic variables meant to be closer linked to the actual impacts of a storm. For example, the proposed ARx-Py scale does not include antecedent moisture, which is known from several studies to be very important for landslide triggering and runoff (Jakob & Weatherly, 2003). Under certain circumstances, an AR could be classified as a strong

or extreme (e.g., AR4-P4) storm, but it may lead to only minor flooding because tree canopies and the forest soil duff layer can absorb substantial volumes of moisture before it is released into the stream network or manifested as landslides. This is particularly important for short duration storms that do not allow overcoming of soil suction (negative pore water pressures) during the storm. For multi-day storms, and those occurring in the fall when preceding rains have partially saturated forest soils, the connection with heavy rain and landslides is more direct. The fluctuating snow levels during a strong AR may also lead to enhanced landslide activity when snowmelt impacts add to already heavy rain amounts. This can modify the timing and location of the most severe impacts, such as with the storm of 28 November 2020 near the Bute Inlet where the landslide originated high in the valley near the snow level during the heaviest precipitation. In addition, landuse and forest state will affect the severity of a given storm in forested mountainous terrain. Areas with clearcuts and poorly constructed forest roads will be more susceptible to landslides and washouts compared to undisturbed terrain. Similarly, areas that have been burned by recent wildfires will respond more readily to heavy rain events. This means that for such areas, the impacts may be at least one category greater than suggested by Fig. 14. Lastly, the current scale does not include shorter duration precipitation (1 hour or less) which is known to be critical for landslide initiation, especially debris flows and debris avalanches (see Jakob & Owen, 2021). In short, moderate rainfall intensities ($< \sim 4\,\mathrm{mm\ h^{-1}}$) may not trigger such landslides as excess pore water pressures cannot develop. That said, many storms embed cells of high intensity rainfall as evidenced by weather radar echos. In addition, other adverse meteorological conditions such as icing, high winds, and rapid snowmelt can also accompany landfalling ARs and can alter their impacts. Development of a more comprehensive scale to address all these issues is desirable, but it is beyond the scope of this paper.

Acknowledgments

Preliminary results from this study were presented at the 2020 AGU Fall Meeting (Mo, 2020). We would like to thank Giselle Bramwell and Johnson Zhong (ECCC) for their help in precipitation and radar data collection, Bobby Sekhon (ECCC) for his weather briefing, and Brian Crenna (ECCC) for his assistance with the AR scale application development. Lin Xu and Chengzhi Ye (Hunan Meteorological Service, China) are acknowledged for their partial support of this study. We also thank Dr. Hai Lin (ECCC) for his

internal review of this study. Editor Stefan Kollet, Associate Editor Rafael Rosolem, and three anonymous reviewers made constructive comments and suggestions for revisions. Some data and computational programs used in this study are accessible from the Federated Research Data Repository at https://doi.org/10.20383/102.0472 (Mo, 2021); Nichole DeMichelis is acknowledged for her assistance in data submission.

Appendix A Specific Humidity and Saturation Specific Humidity

The specific humidity q is a useful quantity in meteorology. It is defined as the mass of water vapor in a unit of moist air. Its value can be either obtained from the NWP model output or calculated from the following relations (Stull, 2017)

$$q = \epsilon e/[p - (1-\epsilon)e], \quad e = \rho_{\rm v} R_{\rm v}(T + 273.15), \tag{A1}$$

where e is the partial pressure due to water vapor (often known as vapor pressure), p is the total air pressure, $\epsilon = 0.622$ is a gas-constant ratio, $\rho_{\rm v}$ is the density of water vapor (absolute humidity), $R_{\rm v} = 461.5\ {\rm J\,K^{-1}kg^{-1}}$ is the gas constant for pure water vapor, and T is the air temperature in Celsius (°C).

The saturation specific humidity $q_{\rm s}$ is the specific humidity corresponding to the maximum amount of water vapor that can exist in air for a given temperature and pressure. It can be calculated using Eq. (A1) with e replaced by the saturation vapor pressure $e_{\rm s}$. Alduchov and Eskridge (1996) recommended the following two equations to calculate $e_{\rm s}$ for moist air above a plane surface of liquid water ($e_{\rm sa}$) or ice ($e_{\rm si}$),

$$e_{\rm sw} = 6.11374 \exp[4.5 \times 10^{-6} p + 17.625\, T/(T + 243.04)], \tag{A2}$$

$$e_{\rm si} = 6.10489 \exp[8 \times 10^{-6} p + 22.587\, T/(T + 273.86)], \tag{A3}$$

In the above equations, the pressure is given in hPa.

Given that supercooled liquid water can exist in the atmosphere with temperatures in the range $-40°{\rm C} < T < 0°{\rm C}$ (Stull, 2017), in this study we calculate $e_{\rm s}$ as a weighted average of $e_{\rm sw}$ and $e_{\rm si}$, i.e.,

$$e_{\rm s} = a_{\rm w} e_{\rm sw} + (1 - a_{\rm w}) e_{\rm si}, \quad \text{with } a_{\rm w} = \begin{cases} 1, & \text{if } T > 0°{\rm C}, \\ (T+40)/40, & \text{if } -40°{\rm C} < T \le 0°{\rm C}, \\ 0, & \text{if } T \le -40°{\rm C}. \end{cases} \tag{A4}$$

Note that, with T replaced by the dewpoint $T_{\rm d}$, the above equations can also be used to calculate the vapor pressure e.

Conflict of Interest

The authors declare no conflicts of interest relevant to this study.

Data Availability Statement

Some data and two Python programs used in this study for calculating the IWV, IVT, CRH, and PCR are publicly available from the Federated Research Data Repository at https://doi.org/10.20383/102.0472.

References

Alduchov, O. A., & Eskridge, R. E. (1996). Improved Magnus form approximation of saturation vapor pressure. *J. Appl. Meteor.*, *35*, 601–609. doi: 10.1175/1520-0450(1996)035⟨0601:IMFAOS⟩2.0.CO;2

American Meteorological Society. (2021). *Glossary of Meteorology*. (Available online at `http://glossary.ametsoc.org/wiki/Atmospheric_river`)

Anthes, R. A. (1977). A cumulus parameterization scheme utilizing a one-dimensional cloud model. *Mon. Wea. Rev.*, *105*, 270–286. doi: 10.1175/1520-0493(1977)105⟨0270:ACPSUA⟩2.0.CO;2

Bao, J.-W., Michelson, S. A., Neiman, P. J., Ralph, F. M., & Wilczak, J. M. (2006). Interpretation of enhanced integrated water vapor bands associated with extratropical cyclones: Their formation and connection to tropical moisture. *Mon. Wea. Rev.*, *134*, 1063–1080. doi: 10.1175/MWR3123.1

Benton, G. S., & Estoque, M. A. (1954). Water-vapor transfer over the North American continent. *J. Meteor.*, *11*, 462–477. doi: 10.1175/1520-0469(1954)011⟨0462:WVTOTN⟩2.0.CO;2

Blamey, R. C., Ramos, A. M., Trigo, R. M., Tomé, R., & Reason, C. J. C. (2018). The influence of atmospheric rivers over the South Atlantic on winter rainfall in South Africa. *J. Hydrometeor.*, *19*, 127–142. doi: 10.1175/JHM-D-17-0111.1

Bretherton, C. S., Peters, M. E., & Back, L. E. (2004). Relationships between water vapor path and precipitation over the tropical oceans. *J. Climate*, *17*, 1517–1528. doi: 10.1175/1520-0442(2004)017⟨1517:RBWVPA⟩2.0.CO;2

Browning, K. A. (1971). Radar measurements of air motion near fronts. Part two: some categories of frontal air motion. *Weather*, *26*, 293–304. doi: 10.1002/j

.1477-8696.1971.tb04211.x

Carlson, T. N. (1980). Airflow through midlatitude cyclones and the comma cloud pattern. *Mon. Wea. Rev.*, *108*, 1498–1509. doi: 10.1175/1520-0493(1980)108⟨1498:ATMCAT⟩2.0.CO;2

Chen, J., Zhang, H., Ye, C., Chen, H., & Mo, R. (2020). Case studies of atmospheric rivers over China and Australia: new insight into their rainfall generation. *J. South. Hemisph. Earth Syst. Sci.*, *70*, 17–35. doi: 10.1071/ES19026

Cordeira, J. M., Ralph, F. M., & Moore, B. J. (2013). The development and evolution of two atmospheric rivers in proximity to western North Pacific tropical cyclones in October 2010. *Mon. Wea. Rev.*, *141*, 4234–4255. doi: 10.1175/MWR-D-13-00019.1

Cruickshank, A. (2019). A river in the sky: Atmospheric rivers are changing. *Star Metro Vancouver*, 31 May, p.1 and p.6. (Available online at `https://projects.thestar.com/climate-change-canada/british-columbia/`)

Dacre, H. F., Clark, P. A., Martinez-Alvarado, O., Stringer, M. A., & Lavers, D. A. (2015). How do atmospheric rivers form? *Bull. Amer. Meteor. Soc.*, *96*, 1243–1255. doi: 10.1175/BAMS-D-14-00031.1

Dettinger, M. (2004). *Fifty-Two Years of "Pineapple-Express" Storms across the West Coast of North America.* U.S. Geological Survey, Scripps Institution of Oceanography for the California Energy Commission, PIER Energy-Related Environmental Research. CEC-500-2005-004. (Available online at `http://www.energy.ca.gov/2005publications/CEC-500-2005-004/CEC-500-2005-004.PDF`)

Espy, J. P. (1841). *The Philosophy of Storms.* Boston, MA, USA: Charles C. Little and James Brown.

Garreaud, R. (2013). Warm winter storms in Central Chile. *J. Hydrometeor.*, *14*, 1515–1534. doi: 10.1175/JHM-D-12-0135.1

Guan, B., & Waliser, D. E. (2015). Detection of atmospheric rivers: Evaluation and application of an algorithm for global studies. *J. Geophys. Res. Atmos.*, *120*, 12514–12535. doi: 10.1002/2014GL060299

Guan, B., & Waliser, D. E. (2019). Tracking atmospheric rivers globally: Spatial distributions and temporal evolution of life cycle characteristics. *J. Geophys. Res. Atmos.*, *124*, 12523–12552. doi: 10.1029/2019JD031205

Harrold, T. W. (1973). Mechanisms influencing the distribution of precipitation within baroclinic disturbances. *Quart. J. R. Met. Soc.*, *99*, 232–251. doi: 10.1002/qj.49709942003

Hatchett, B. J., Cao, Q., Dawson, P. B., Ellis, C. J., Hecht, C. W., Kawzenuk, B., ... Sumargo, E. (2020). Observations of an extreme atmospheric river storm with a diverse sensor network. *Earth Space Sci.*, *6*, e2020EA001129. doi: 10.1029/2020EA001129

Houghton, H. G. (1951). On the physics of clouds and precipitation. In T. F. Malone (Ed.), *Compendium of meteorology* (pp. 165–181). Boston, MA, USA: Amer. Meteor. Soc. doi: 10.1007/978-1-940033-70-9_14

Huang, Z. (2020). Sichan floods lead to mass evacuation. *China Daily (Hong Kong Edition)*, 18 August, Page 4. (Available online at `https://www.chinadailyhk.com/epaper/pubs//chinadaily/2020/08/18/04.pdf`)

Jacob, D. (2001). The role of water vapour in the atmosphere. A short overview from a climate modeller's point of view. *Phys. Chem. Earth*, *26A*, 523–527. doi: 10.1016/S1464-1895(01)00094-1

Jakob, M., & Owen, T. (2021). Climate change effects on landslides in the North Shore Mountains of Vancouver. *Geomorphology*, In print.

Jakob, M., & Weatherly, H. (2003). A hydroclimatic threshold for landslide initiation on the North Shore Mountains of Vancouver, British Columbia. *Geomorphology*, *54*, 137–156. doi: 10.1016/S0169-555X(02)00339-2

Jones, N. (2021). Massive landslide cools fjord. *Hakai Magazine*. (Published online at `https://www.hakaimagazine.com/news/massive-landslide-cools-fjord/`)

Kuo, H.-L. (1974). Further studies of the parameterization of the influence of cumulus convection on large-scale flow. *J. Atmos. Sci.*, *31*, 1232–1240. doi: 10.1175/1520-0469(1974)031⟨1232:FSOTPO⟩2.0.CO;2

Lavers, D. A., Allan, R. P., Wood, E. F., Villarini, G., Brayshaw, D. J., & Wade, A. J. (2011). Winter floods in Britain are connected to atmospheric rivers. *Geophys. Res. Lett.*, *38*, L23803. doi: 10.1029/2011GL049783

Lavers, D. A., Villarini, G., Allan, R. P., Wood, E. F., & Wade, A. J. (2012). The detection of atmospheric rivers in atmospheric reanalyses and their links to British winter floods and the large-scale climatic circulation. *J. Geophys. Res.*

Atmos., *117*, D20106. doi: 10.1029/2012JD018027

Li, Y., Szeto, K., Stewart, R. E., Thériault, J. M., Chen, L., Kochtubajda, B., ... Kurkute, S. (2017). A numerical study of the June 2013 flood-producing extreme rainstorm over southern Alberta. *J. Hydrometeor.*, *18*, 2057–2078. doi: 10.1175/JHM-D-15-0176.1

Liu, A. Q., Mooney, C., Szeto, K., Thériault, J. M., Kochtubajda, B., Stewart, R. E., ... Pomeroy, J. (2016). The June 2013 Alberta catastrophic flooding event: Part 1–Climatological aspects and hydrometeorological features. *Hydrol. Process.*, *30*, 4899–4916. doi: 10.1002/hyp.10906

Lu, A. (1947). Precipitation in the South Chinese-Tibetan borderland. *Geog. Rev.*, *37*, 88–93. doi: 10.2307/211363

Mahoney, K., Jackson, D. L., Neiman, P., Hughes, M., Darby, L., Wick, G., ... Cifelli, R. (2016). Understanding the role of atmospheric rivers in heavy precipitation in the Southeast United States. *Mon. Wea. Rev.*, *144*, 1617–1632. doi: 10.1175/MWR-D-15-0279.1

Manabe, S., & Wetherald, R. T. (1967). Thermal equilibrium of the atmosphere with a given distribution of relative humidity. *J. Atmos. Sci.*, *24*, 241–259. doi: 10.1175/1520-0469(1967)024⟨0241:TEOTAW⟩2.0.CO;2

Marshall, J. S., & Palmer, W. M. (1948). The distribution of raindrops with size. *J. Meteor.*, *5*, 165–166. doi: 10.1175/1520-0469(1948)005⟨0165:TDORWS⟩2.0.CO;2

McEwen, G. F. (1930). Our rainfall: how is it formed and what becomes of it? *Sci. Monthly*, *31*, 385–400. doi: 10.2307/15005

McTaggart-Cowan, R., Vaillancourt, P. A., Zadra, A., Chamberland, S., Charron, M., Corvec, S., ... Yang, J. (2019). Modernization of atmospheric physics parameterization in Canadian NWP. *J. Adv. Model. Earth Syst.*, *11*, 3593–3635. doi: 10.1029/2019MS001781

Millar, K.-J. (2020). "Don't put away your rain gear": Environment Canada. *Prince Rupert Northern View*, *14*, 20 August, A3. (Also see on A2: Dozens stranded after landslides block roads into Work Channel site; available online at `https://www.thenorthernview.com/e-editions/?pub_code=pru&&container=p20110819100700000&&date=2020-08`)

Mo, R. (2016). Atmospheric rivers in the Northeast Pacific: Pineapple Express.

In *Meteorology Today: An Introduction to Weather, Climate, and the Environment* (2nd Canadian ed., pp. 360–361). C. D. Ahrens, P. L. Jackson, and C. E. O. Jackson, Nelson Education Ltd.

Mo, R. (2020). Diagnosing primary condensation rate attributed to the moisture convergence: Applications to atmospheric river analysis and extratropical storm classification. A117-0004, presented at 2020 Fall Meeting, AGU, 1-17 December. doi: 10.1002/essoar.10505440.1

Mo, R. (2021). Meteorological data for three atmospheric river case studies and Python programs for calculating column relative humidity and primary condensation rate. *Federated Research Data Repository*. doi: 10.20383/102.0472

Mo, R., Brugman, M. M., Milbrandt, J. A., Goosen, J., Geng, Q., Emond, C., ... Erfani, A. (2019). Impacts of hydrometeor drift on orographic precipitation: Two case studies of landfalling atmospheric rivers in British Columbia, Canada. *Wea. Forecasting*, *34*, 1211–1237. doi: 10.1175/WAF-D-18-0176.1

Mo, R., & Lin, H. (2019). Tropical–mid-latitude interactions: Case study of an inland-penetrating atmospheric river during a major winter storm over North America. *Atmos.-Ocean*, *57*, 208–232. doi: 10.1080/07055900.2019.1617673

Neiman, P. J., Ralph, F. M., Wick, G. A., Lundquist, J. D., & Dettinger, M. D. (2008). Meteorological characteristics and overland precipitation impacts of atmospheric rivers affecting the west coast of North America based on eight years of SSM/I satellite observations. *J. Hydrometeor.*, *9*, 22–47. doi: 10.1175/2007JHM855.1

Newell, R. E., Newell, N. E., Zhu, Y., & Scott, C. (1992). Tropospheric rivers? – A pilot study. *Geophys. Res. Lett.*, *19*, 2401–2404. doi: 10.1029/92GL02916

Paltan, H., Waliser, D., Lim, W. H., Guan, B., Yamazaki, D., Pant, R., & Dadson, S. (2017). Global floods and water availability driven by atmospheric rivers. *Geophys. Res. Lett.*, *44*. doi: 10.1002/2017GL074882

Pan, M., & Lu, M. (2019). A novel atmospheric river identification algorithm. *Water Resour. Res.*, *55*, 6069–6087. doi: 10.1029/2018WR024407

Peixoto, J. P. (1973). *Atmospheric Vapour Flux Computations for Hydrological Purposes* (Reports on WMO/IHD Projects, No. 20). Geneva, Switzerland: World Meteorological Organization.

Pollon, C. (2021). The Bute Inlet disaster: How dying glaciers can unleash devasta-

tion. *The Tyee*. (Published online at `https://thetyee.ca/News/2021/05/17/Bute-Inlet-Disaster-Dying-Glaciers-Unleash-Devastation/`)

Ralph, F. M., Neiman, P. J., & Wick, G. A. (2004). Satellite and CALJET aircraft observations of atmospheric rivers over the eastern North Pacific Ocean during the winter of 1997/98. *Mon. Wea. Rev.*, *132*, 1721–1745. doi: 10.1175/1520-0493(2004)132⟨1721:SACAOO⟩2.0.CO;2

Ralph, F. M., Rutz, J. J., Cordeira, J. M., Dettinger, M., Anderson, M., Reynolds, D., ... Smallcomb, C. (2019). A scale to characterize the strength and impacts of atmospheric rivers. *Bull. Amer. Meteor. Soc.*, *100*, 269–289. doi: 10.1175/BAMS-D-18-0023.1

Rossby, C.-G., & Collaborators. (1937). Aerological evidence of large-scale mixing in the atmosphere. *Eos, Trans. Amer. Geophys. Union*, *18*, 130–136. doi: 10.1029/TR018i001p00130-2

Rutz, J. J., Steenburgh, W. J., & Ralph, F. M. (2014). Climatological characteristics of atmospheric rivers and their inland penetration over the western United States. *Mon. Wea. Rev.*, *142*, 905–921. doi: 10.1175/MWR-D-13-00168.1

Schneider, T., O'Gorman, P. A., & Levine, X. J. (2010). Water vapor and the dynamics of climate changes. *Rev. Geophys.*, *48*, RG3001. doi: 10.1029/2009RG000302

Sharma, A. R., & Déry, S. J. (2020). Contribution of atmospheric rivers to annual, seasonal, and extreme precipitation across British Columbia and southeastern Alaska. *J. Geophys. Res. Atmos.*, *125*(9), e2019JD031823. doi: 10.1029/2019JD031823

Shields, C. A., Rutz, J. J., Leung, L.-Y., Ralph, F. M., Wehner, M., Kawzenuk, B., ... Nguyen, P. (2018). Atmospheric River Tracking Method Intercomparison Project (ARTMIP): project goals and experimental design. *Geosci. Model Dev.*, *11*, 2455–2474. doi: 10.5194/gmd-11-2455-2018

Shih, G. (2020). Floods devastate China's Yangtze basin as army mobilizes massive relief effort. *The Washington Post*, 22 August, Page A14. (Available online at `https://www.washingtonpost.com/world/asia_pacific/china-floods-emergency-rescue-military-sichuan-economy/2020/08/21/668ed212-e35b-11ea-82d8-5e55d47e90ca_story.html`)

Sodemann, H., & Stohl, A. (2013). Moisture origin and meridional transport in at-

mospheric rivers and their association with multiple cyclones. *Mon. Wea. Rev.*, *141*, 2850–2868. doi: 10.1175/MWR-D-12-00256.1

Starr, V. P., & Peixoto, J. P. (1958). On the global balance of water vapor and the hydrology of deserts. *Tellus*, *10*, 188–194. doi: 10.1111/j.2153-3490.1958.tb02004.x

Stohl, A., & James, P. (2004). A Lagrangian analysis of the atmospheric branch of the global water cycle. Part I: Method description, validation, and demonstration for the August 2002 flooding in central Europe. *J. Hydrometeor.*, *5*, 656–678. doi: 10.1175/1525-7541(2004)005⟨0656:ALAOTA⟩2.0.CO;2

Stull, R. (2017). *Practical Meteorology: An Algebra-based Survey of Atmospheric Science*. Vancouver, BC, Canada: University of British Columbia. (Available online at `https://www.eoas.ubc.ca/books/Practical_Meteorology/`)

Sundqvist, H. (1978). A parameterization scheme for non-convective condensation including prediction of cloud water content. *Quart. J. R. Met. Soc.*, *104*, 677–690. doi: 10.1002/qj.49710444110

Sundqvist, H., Berge, E., & Kristjánsson, J. E. (1989). Condensation and cloud parameterization studies with a mesoscale numerical weather prediction model. *Mon. Wea. Rev.*, *117*, 1641–1657. doi: 10.1175/1520-0493(1989)117⟨1641:CACPSW⟩2.0.CO;2

Tan, Y., & Li, H. (2020). Chongqing flooding considered among worst city has ever seen. *China Daily (Hong Kong Edition)*, 21 August, Page 3. (Available online at `https://www.chinadailyhk.com/epaper/pubs//chinadaily/2020/08/21/03.pdf`)

Trenberth, K. E., & Guillemot, C. J. (1998). Evaluation of the atmospheric moisture and hydrological cycle in the NCEP/NCAR reanalyses. *Clim. Dyn.*, *14*, 213–231. doi: 10.1007/s003820050219

Tuller, S. E. (1971). The world distribution of annual precipitation efficiency. *J. Geography*, *70*, 219–223. doi: 10.1080/00221347108981623

Tuller, S. E. (1973). Seasonal and annual precipitation efficiency in Canada. *Atmosphere*, *11*, 52–66. doi: 10.1080/00046973.1973.9648348

Tyndall, J. (1863). On radiation through the earth's atmosphere. *London Edinburgh Dublin Philos. Mag. J. Sci.*, *25*, 200-206. doi: 10.1080/14786446308643443

Wick, G. A., Neiman, P. J., & Ralph, F. M. (2013). Description and validation of

an automated objective technique for identification and characterization of the integrated water vapor signature of atmospheric rivers. *IEEE Trans. Geosci. Remote Sens.*, *51*, 2166–2176. doi: 10.1109/TGRS.2012.2211024

Xiong, Y., & Ren, X. (2021). Influences of atmospheric rivers on North Pacific winter precipitation: Climatology and dependence on ENSO condition. *J. Climate*, *34*, 277–292. doi: 10.1175/JCLI-D-20-0301.1

Ye, C., Zhang, H., Moise, A., & Mo, R. (2020). Atmospheric rivers in the Australia-Asian region: a BoM-CMA collaborative study. *J. South. Hemisph. Earth Syst. Sci.*, *70*, 3–16. doi: 10.1071/ES19025

Zhang, W., Huang, Z., Jiang, F., Stuecker, M. F., Chen, G., & Jin, F.-F. (2021). Exceptionally persistent Madden-Julian Oscillation activity contributes to the extreme 2020 East Asian summer monsoon rainfall. *Geophy. Res. Lett.*, *48*, e2020GL091588. doi: 10.1029/2020GL091588

Zhang, Z., Ralph, F. M., & Zheng, M. (2019). The relationship between extratropical cyclone strength and atmospheric river intensity and position. *Geophys. Res. Lett.*, *46*, 1814–1823. doi: 10.1029/2018GL079071

Zhao, M. (2020). Simulations of atmospheric rivers, their variability, and response to global warming using GFDL's new high-resolution general circulation model. *J. Climate*, *33*, 10287–10303. doi: 10.1175/JCLI-D-20-0241.1

Zheng, M., Delle Monache, L., Wu, X., Ralph, F. M., Cornuelle, B., Tallapragada, V., ... others (2021). Data gaps within atmospheric rivers over the northeastern Pacific. *Bull. Amer. Meteor. Soc.*, *102*, E492–E524. doi: 10.1175/BAMS-D-19-0287.1

Zhou, Z.-Q., Xie, S.-P., & Zhang, R. (2021). Historic Yangtze flooding of 2020 tied to extreme Indian Ocean conditions. *Proc. Nat. Acad. Sci.*, *118*. doi: 10.1073/pnas.2022255118

Zhu, Y., & Newell, R. E. (1994). Atmospheric rivers and bombs. *Geophys. Res. Lett.*, *21*, 1999–2002. doi: 10.1029/94GL01710

Zhu, Y., & Newell, R. E. (1998). A proposed algorithm for moisture fluxes from atmospheric rivers. *Mon. Wea. Rev.*, *126*, 725–735. doi: 10.1175/1520-0493(1998)126⟨0725:APAFMF⟩2.0.CO;2

Zhu, Y., Newell, R. E., & Read, W. G. (2000). Factors controlling upper-troposphere water vapor. *J. Climate*, *13*, 836–848. doi: 10.1175/1520-0442(2000)013⟨0836:

FCUTWV⟩2.0.CO;2